THE ASTROPHYSICAL JOURNAL, 472:760–782, 1996 December 1

CONSTRAINTS ON STELLAR GRAIN FORMATION FROM PRESOLAR GRAPHITE IN THE MURCHISON METEORITE

THOMAS J. BERNATOWICZ,[1,2,3] RAMANATH COWSIK,[1,2,4] PATRICK C. GIBBONS,[2] KATHARINA LODDERS,[3,5] BRUCE FEGLEY, JR.,[1,3,5] SACHIKO AMARI,[1,6] AND ROY S. LEWIS[6]
Received 1996 February 7; accepted 1996 June 11

ABSTRACT

We report the results of isotopic, chemical, structural, and crystallographic microanalyses of graphitic spherules (0.3–9 μm) extracted from the Murchison meteorite. The spherules have $^{12}C/^{13}C$ ratios ranging over 3 orders of magnitude (from 0.02 to 80 times solar), clearly establishing their presolar origin as stellar condensates. These and other isotopic constraints point to a variety of stellar types as sources of the carbon, including low-mass asymptotic giant branch (AGB) stars and supernovae. Transmission electron microscopy (TEM) of ultrathin sections of the spherules revealed that many have a composite structure consisting of a core of nanocrystalline carbon surrounded by a mantle of well-graphitized carbon. The nanocrystalline cores are compact masses consisting of randomly oriented graphene sheets, from PAH-sized units up to sheets 3–4 nm in diameter, with little graphitic layering order. These sheets probably condensed as isolated particles that subsequently coalesced to form the cores, after which the surrounding graphitic mantles were added by vapor deposition.

We also detected internal crystals of metal carbides in one-third of the spherules. These crystals (5–200 nm) have compositions ranging from nearly pure TiC to nearly pure Zr-Mo carbide. Some of these carbides occur at the centers of the spherules and are surrounded by well-graphitized carbon, having evidently served as heterogeneous nucleation centers for condensation of carbon. Others were entrained by carbon as the spherules grew. The chemical and textural evidence indicates that these carbides formed prior to carbon condensation, which indicates that the C/O ratios in the stellar sources were very close to unity. Only one of the 67 spherules studied in the TEM contained SiC, from which we infer that carbon condensation nearly always preceded SiC formation. This observation places stringent limits on the possible delay of graphite formation and is consistent with the predictions of equilibrium thermodynamics in the inferred range of pressure and C/O ratios.

We model the formation of the observed refractory carbides under equilibrium conditions, both with and without *s*-process enrichment of Zr and Mo, and show that the chemical variation among internal crystals is consistent with the predicted equilibrium condensation sequence. The compositions of most of the Zr-Mo-Ti carbides require an *s*-process enrichment of both Zr and Mo to at least 30 times their solar abundances relative to Ti. However, to account for crystals in which Mo is also enriched relative to Zr, it is necessary to suppose that Zr is removed by separation of the earliest formed ZrC crystals from their parent gas.

We also explore the formation constraints imposed by kinetics, equilibrium thermodynamics, and the observation of clusters of carbide crystals in some spherules, and conclude that relatively high formation pressures ($\gtrsim 0.1$ dynes cm^{-2}), and/or condensable carbon number densities ($\gtrsim 10^8$ cm^{-3}) are required. The graphite spherules with $^{12}C/^{13}C$ ratios less than the solar value may have originated in AGB stellar winds. However, in the spherically symmetric AGB atmospheres customarily assumed in models of stellar grain formation, pressures are much too low (by factors of $\gtrsim 10^2$) to produce carbide crystals or graphite spherules of the sizes observed within plausible timescales. If some of the graphite spherules formed in the winds from such stars, it thus appears necessary to assume that the regions of grain formation are density concentrations with length scales less than a stellar radius. Some of the spherules with both $^{12}C/^{13}C$ ratios greater than the solar value and ^{28}Si excesses probably grew in the ejecta of supernovae. The isotopic compositions and growth constraints imply that they must have formed at high densities (e.g., with $\rho \gtrsim 10^{-12}$ g cm^{-3}) from mixtures of inner-shell material with material from the C-rich outer zones.

Subject headings: dust, extinction — interplanetary medium — ISM: abundances — meteors, meteoroids — nuclear reactions, nucleosynthesis, abundances

[1] McDonnell Center for the Space Sciences, Washington University, St. Louis, MO 63130.
[2] Department of Physics, Washington University, St. Louis, MO 63130.
[3] Department of Earth and Planetary Sciences, Washington University, St. Louis, MO 63130.
[4] Indian Institute of Astrophysics, Bangalore-560036, India.
[5] Planetary Chemistry Laboratory, Washington University, St. Louis, MO 63130.
[6] Enrico Fermi Institute, University of Chicago, Chicago IL 60637.

1. INTRODUCTION

In recent years, the study of circumstellar and supernova grains extracted from primitive meteorites has provided a rich new source of information on stellar nucleosynthesis.[7] The development of elaborate physical and chemical separation techniques (Amari, Lewis, & Anders 1994) has led to the isolation of circumstellar grains large enough to be individually studied, including silicon carbide (Bernatowicz et al. 1987; Tang & Anders 1988), graphite (Amari et al. 1990, 1993), titanium carbide (Bernatowicz et al. 1991), corundum (Huss et al. 1994; Nittler et al. 1994), and silicon nitride (Hoppe et al. 1994; Nittler et al. 1995). Advances in secondary ion mass spectrometry techniques have permitted the measurement of isotopic compositions of major and minor elements in *individual* micron-sized grains, allowing circumstellar grains to be distinguished from the bulk of the meteoritic material that was formed or reprocessed within the solar nebula. The isotopic information gleaned from such studies has been used to test models of nucleosynthesis in unprecedented detail, prompting more sophisticated theoretical treatment. In some cases such studies have led to the identification of the kinds of astrophysical sites where the grains originated. For example, on the basis of the isotopic composition of both major and minor elements, we can assert that most silicon carbide grains present in the early solar nebula originated in the atmospheres of asymptotic giant branch (AGB) stars, but that some ($\sim 1\%$) were formed in supernova ejecta (Anders & Zinner 1993; Ott 1993; Amari et al. 1995d).

The study of circumstellar grains from meteorites provides an equally novel pathway to a different kind of astrophysical information. The detailed characterization of these grains can yield information on pressure, temperature, and chemical compositions in stellar atmospheres and ejecta. For example, in a transmission electron microscopy (TEM) study of presolar graphite from the Murchison meteorite, Bernatowicz et al. (1991) identified the refractory phase, titanium carbide (TiC, a species not previously observed in meteorites), within the graphite. On the basis of textural and crystallographic evidence, these authors concluded that the TiC had condensed first and was occluded by the graphite. Calculations of condensation under equilibrium conditions (e.g., Larimer 1975; Lattimer, Schramm, & Grossman 1978; Larimer & Bartholomay 1979) for gases with C/O > 1 had indeed predicted that TiC and graphite are the first-formed condensates of major elements over a wide range of gas pressures. More recent models that thoroughly explore the parameter space of temperature, pressure, and C/O ratio (e.g., Sharp & Wasserburg 1995; Lodders & Fegley 1993, 1995) show that the formation of TiC occurs before that of graphite for C/O ratios between 1.05 and 1.2 at astrophysically plausible pressures. This result is consistent with C/O ratios in the atmospheres of carbon stars inferred from astronomical observations (Lambert et al. 1986; Olofsson et al. 1993).

In conventional astronomical studies, size distributions and compositions of grains in circumstellar atmospheres must be inferred through physical models and/or comparison with spectra from laboratory analogs. The circumstellar origin of grains from meteorites, on the other hand, can be established by direct isotopic measurement of individual particles. Additional microanalysis by TEM and other techniques can then yield detailed information on circumstellar grain size and morphology, crystallography, and major and minor element composition. The study of circumstellar grains from meteorites is thus a new type of astrophysics and a powerful complement to astronomical observations, allowing us to obtain a more complete picture of stellar atmosphere chemistry and grain condensation. It is worth noting in this regard that because some of the major elements in these grains have low cosmic abundances (e.g., Ti in TiC), the chance for astronomically observing such grains is very slight.

Here we report the results of microanalyses of circumstellar graphite spherules extracted from the Murchison carbonaceous chondrite. In § 2 we discuss the external morphology, size distribution, and isotopic characteristics of the spherules, and what the latter indicate about the kinds of stellar environments in which the spherules formed. We next describe the internal structure of the spherules as revealed by TEM analyses (§ 3), and show that the spherules frequently have cores of nanocrystalline carbon mantled by well-graphitized carbon. We also discuss the results of detailed electron diffraction and electron energy loss analyses used to characterize the nanocrystalline carbon core material. In § 4 we draw some broad inferences concerning the development of the nanocrystalline core-graphite mantle structure of the circumstellar graphite spherules. In § 5 we describe crystals of refractory Ti-, Zr-, and Mo-bearing carbides that occur within the spherules and have sometimes served as nucleation centers for graphite growth. These carbides have remained cloaked in a protective covering of graphite since their formation, and thus provide direct information on the physical and chemical properties of carbon-bearing circumstellar condensates. We then use these observations, in conjunction with detailed equilibrium condensation (§ 6) and grain formation models (§ 7), to extract information about the physical conditions in stellar grain formation environments.

2. PHYSICAL AND ISOTOPIC CHARACTERIZATION OF PRESOLAR GRAPHITE

2.1. *Samples and Experimental Methods*

We studied graphite spherules from the Murchison meteorite graphite separate KFC1 (2.15–2.20 g cm^{-3}), whose preparation has been described in detail by Amari et al. (1994). Carbon isotopic data obtained by ion microprobe analysis of individual graphite spherules from KFC1 were reported by Amari et al. (1993) and Hoppe et al. (1995); results for 202 spherules are summarized in Figure 1. Presolar graphite occurs in two morphological types, resembling either cauliflowers or onions in external appearance (e.g., Zinner et al. 1995). Both cauliflower and onion types of graphite spherules are present in KFC1, the latter comprising 84% of the total; for the remainder of this paper we will consider only this kind of graphite. The $^{12}C/^{13}C$ ratios of the onion-type graphite range over 3 orders of magnitude, with values from 0.02 to 80 times the solar ratio of 89. Only a small fraction ($\sim 5\%$) of the graphitic spherules have a solar $^{12}C/^{13}C$ ratio within analytical uncertainty: 70% have ratios in excess of the solar value, and 25% have smaller ratios. These isotopic data are convincing evidence of the

[7] For convenience we will hereafter use the term "circumstellar grain" to refer to solids condensed in any kind of stellar outflow, including supernovae ejecta.

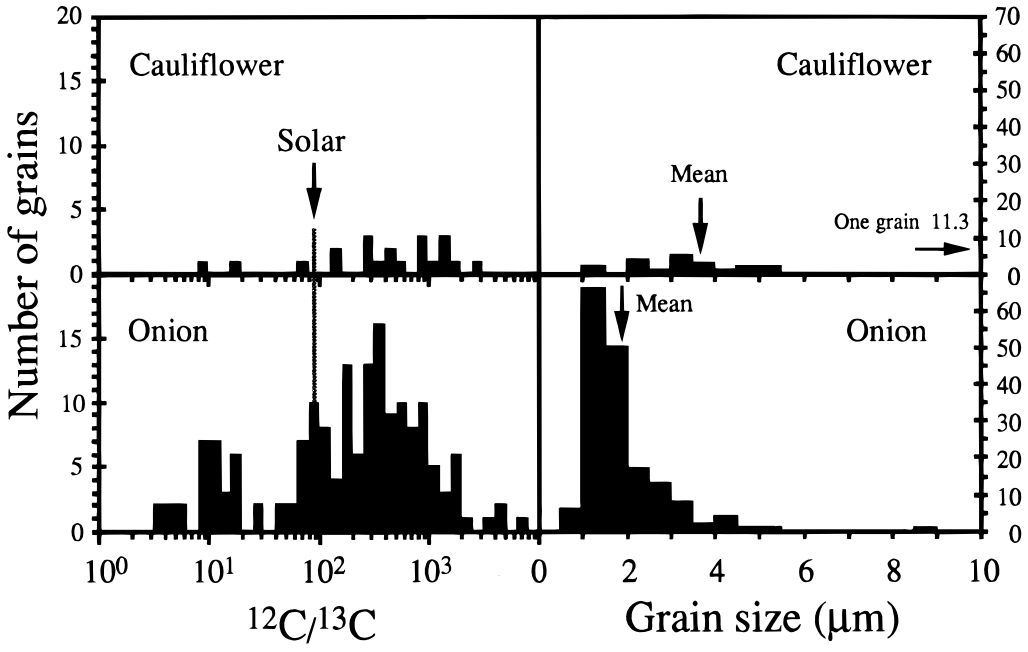

FIG. 1.—Histograms of carbon isotopic compositions and grain diameters of cauliflower- and onion-type circumstellar graphite spherules from the Murchison chondrite. The generally large difference between $^{12}C/^{13}C$ ratios in individual grains and the solar ratio, and the enormous range of these isotopic compositions (over 3 orders of magnitude), clearly establish the presolar origin of these spherules.

presolar origin of most of the graphite, and give assurance that any random sample of these graphites will consist almost entirely of circumstellar grains, which is key to the experimental procedure adopted here.

Sizes of spherules range from a few tenths of a micron up to nearly 10 μm, with a number-weighted mean diameter in the range 1–2 μm and modal diameter of about 1.5 μm (Fig. 1). Figure 2 (Plate 16) is a representative scanning electron microscope photograph of an onion-type spherule, showing the distinctive near-spherical shape and graphitic shell structure.

In a previous study of five presolar graphites from the Murchison chondrite (Bernatowicz et al. 1991), each particle was isotopically characterized by ion microprobe analysis prior to TEM analysis. This procedure yields the maximum amount of information on individual grains. However, candidate grains for TEM analysis (especially very small ones less than 2 μm in diameter) may be completely sputtered away during isotopic analysis, or grains may be lost during the removal and embedding procedure required for TEM analysis. For the present work we have adopted the alternative strategy of TEM study of *suites* of grains; for general isotopic characterization we rely on the previously cited results of ion probe analyses of large numbers of individual graphite spherules. This approach has the disadvantage that the mineralogical characteristics of individual graphites cannot be directly correlated with the isotopic characteristics, but it also has the advantage that many more particles can be studied.

In the preparation for the TEM study, an 8 mm diameter gelatin cylinder was affixed to a precleaned glass slide with RTV silicone cement. Presolar graphite particles were then deposited from suspension in an area of less than 1 mm^2 on the glass within the cylinder; the deposit was dried, embedded in LR White hard resin (which was detached from the slide after curing), and sliced into sections $\lesssim 100$ nm thick with an ultramicrotome equipped with a diamond knife. Each of these slices contained ultrathin sections of many graphite spherules. The slices were retrieved on Cu TEM grids covered with holey C films, and were examined for the composition and structure of their graphite sections in a JEOL-2000FX TEM equipped with a Gatan 666 parallel detection electron spectrometer (PEELS) and a Noran Pioneer X-ray detector (EDS) with a Norvar window sensitive to elements with $Z \geq 5$. A total of 67 spherules was studied.

2.2. *Stellar Sources*

The widely ranging $^{12}C/^{13}C$ ratios (§ 2.1; Fig. 1), as well as a variety of other isotopic data, point to a multiplicity of stellar sources for the graphite spherules. The isotopic composition of *s*-process Kr detected in *bulk* graphite samples (Amari, Lewis, & Anders 1995b) suggests that at least some of the spherules originated in low-mass (1–2 $M_\odot$) AGB stars of low metallicity. But it is unlikely that *all* of the graphite could have originated in carbon-rich AGB stars, because cool carbon (N-type) stars generally have $^{12}C/^{13}C$ ratios less than the solar value of 89, whereas 70% of the graphite spherules have $^{12}C/^{13}C$ ratios greater than this (cf. Fig. 1). Some hydrogen-deficient and CH stars (Fujita & Tsuji 1977; Tsuji et al. 1991) have isotopically light C and are thus a possible source of some of these spherules.

Elements other than carbon are generally too scarce to permit isotopic characterization of them in individual spherules, but ion microprobe measurements have revealed excesses of $^{29,30}Si$, $^{42,43}Ca$ and $^{46,49}Ti$ in some of the spherules, indicative of slow neutron capture in the He-burning shells of AGB or massive stars (Anders & Zinner 1993; Hoppe et al. 1995). Some spherules have ^{28}Si excesses that clearly point to their origin in explosive nucleosynthesis (Meyer, Weaver, & Woosley 1995; Amari, Zinner, & Lewis 1995c). It is likely that these spherules condensed in supernovae ejecta after mixing of material from deep interior stellar zones (where O is burned to ^{28}Si) with C-rich outer

shell material. In the He/C shell of the presupernova star the carbon is isotopically light; thus supernovae are the source of at least some, and perhaps the majority, of the graphite spherules with $^{12}C/^{13}C$ ratios greater than the solar value.

The low $^{20}Ne/^{22}Ne$ ratios measured in bulk samples (Amari et al. 1995b) suggest novae as a third possible stellar source; however, novae are expected to produce very low $^{12}C/^{13}C$ ratios, and, if so, they probably contribute only a small fraction of the graphites (cf. Fig. 1).

3. INTERNAL STRUCTURE OF CIRCUMSTELLAR GRAPHITE SPHERULES

In this section we discuss what microanalysis has revealed about the nature of the carbonaceous matter in circumstellar graphite spherules. High-resolution TEM imaging of ultrathin sections of the spherules directly confirms the implication of SEM photographs (Fig. 2) and the results of laser Raman analysis (Zinner et al. 1995), which indicated that shells of well-ordered graphite constitute the externally sensible parts of the spherules. As viewed in the TEM, the outer parts of the spherules are gently curved graphitic planes that are continuous over hundreds of nanometers. Electron diffraction analysis [using the invariant (100) and (110) reflections for internal calibration of diffraction patterns] shows that the interlayer (002) d-spacings are at most 5% larger than those of perfect hexagonal graphite ($d_{002} = 0.3354$ nm), indicative of well-graphitized carbon (cf. Rietmeijer & Mackinnon 1985).

The TEM studies have revealed two new and important features of the spherules which were *not* apparent from the previous studies. One is the presence of internal crystals of refractory carbide minerals in many of the graphites. These sometimes occur in the center of the spherules, having evidently served as sites for graphite condensation; in other cases they are randomly distributed within the spherules, indicating that they were occluded as carbon condensed. Discussion of these internal crystals is taken up in § 5. The second feature revealed by TEM analysis is the presence of cores of poorly ordered carbonaceous material enclosed by the graphitic shells, which occur in more than 80% of the onion-type graphites studied. The existence of these cores clearly implies that many of the spherules did not start to condense as well-graphitized carbon. For the remainder of this section we describe the results of our efforts to characterize the nature of this core material.

3.1. *Electron Diffraction Analysis and Simulations*

Here we discuss what electron diffraction in the transmission electron microscope reveals about the carbon structures and the degree of crystalline order in the circumstellar graphite spherules. A TEM image of an onion-type graphite with a prominent core is shown in Figure 3 (Plate 17). The outer layers appear dark because electrons diffracted from (002) graphite planes do not pass through the microscope objective aperture; this coherent scattering is very much reduced or absent in the core material, which consequently appears lighter. Selected area diffraction (SAD) of the carbonaceous cores results in diffraction *rings* rather than discrete diffraction spots, a characteristic of randomly oriented, fine-grained crystalline aggregates. To quantify the SAD rings, we digitized TEM negatives and used a profile of the intensity distribution that included the center of the electron diffraction pattern. In Figure 4*a* we display

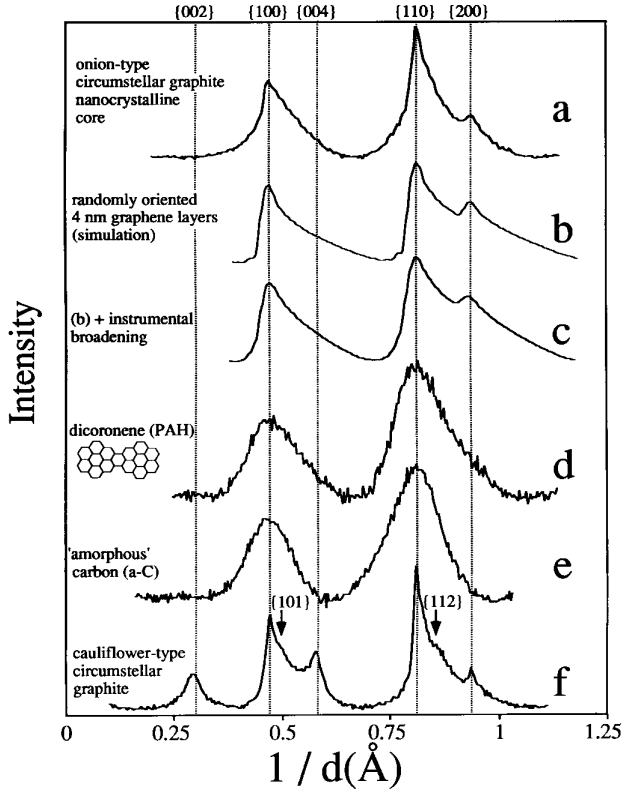

FIG. 4.—TEM electron diffraction intensity profiles for (*a*) a nanocrystalline carbon core of a circumstellar graphite spherule; (*d*) the polycyclic aromatic hydrocarbon (PAH) dicoronene ($C_{48}H_{20}$); (*e*) black amorphous carbon (a-C); and (*f*) turbostratic graphite from a cauliflower-type circumstellar graphite spherule. Note the asymmetry of the {100} and {110} diffraction peaks in the core material (*a*), as well as the lack of any {002} graphite layering reflection. Profiles in (*b*) and (*c*) are numerical simulations of electron scattering intensity distributions for 4 nm randomly oriented graphene sheets. In (*c*), the effect of instrumental broadening has been simulated.

the SAD intensity distribution for the core of the graphite spherule shown in Figure 3, with the diffuse scattering background removed. Comparison of this diffraction pattern with that from a cauliflower-type graphite spherule (Fig. 4*f*) is instructive. Although the cauliflower-type spherule consists entirely of turbostratic graphite (i.e., graphite with contorted layers having no long-range continuity; see Bernatowicz et al. 1991), {00*l*} layering reflections are nonetheless present, as well as {*hkl*} reflections from atomic planes that intersect the unique crystallographic direction. However, the core material (Fig. 4*a*) produces only {*hk*0} and {*h*00} in-plane reflections and an apparent absence of {00*l*} and {*hkl*} layering reflections. The diffraction intensities of the in-plane reflections are markedly tailed toward larger scattering angles, although the positions of the peak maxima for these reflections correspond to the d-spacings of graphite.

We interpret these results to mean that the core material is comprised of sheets of carbon atoms, each consisting of a planar network of aromatic hexagonal rings, hereafter referred to as "graphene." Ordinary graphite consists of large graphene sheets, ordered in the third dimension by regular stacking. Further, a given graphene sheet is laterally shifted relative to the sheets immediately below it and above it (by 0.142 nm), so that the stacking order may be represented by an *ABAB* ... sequence. However, the graphenes

in the core material apparently have little or none of this three-dimensional stacking order, and the individual sheets are quite small. The pattern of electron reflections from the core material is similar to that expected of a collection of randomly oriented *two-dimensional* crystal lattices. By "randomly oriented" we mean that not only are the graphene planes uniformly distributed in all azimuthal orientations, but also that the normals to these planes are isotropically distributed in space. The distribution of scattered intensity from two-dimensional lattices was first described by von Laue (1932), and a complete analytical solution to the problem was derived by Warren (1941). His solution shows that the diffraction peak intensity rises rapidly for a given reflection, but then decreases more gradually toward larger scattering angles, yielding asymmetrical peak shapes just as we observe for the spherule cores (Fig. 4*a*).

To evaluate the extent of stacking order permitted by our diffraction data, we carried out numerical electron scattering simulations. The procedure used was to compute atomic positions in a single, perfect graphene layer within a circle of a given diameter. These coordinates were used to calculate (cf. Warren 1990) a diffracted intensity averaged over all orientations:

$$I = \sum_m \sum_n f_m f_n \frac{\sin(qr_{mn})}{qr_{mn}}, \quad (1)$$

where r_{mn} is the scalar separation between atoms m and n, and f_m is the Lenz-Wentzel electron scattering form factor (Reimer 1989) for atom m evaluated at scattering wavenumber q, with $q = 2\pi/d$ for direct lattice spacing d.

For randomly oriented graphene sheets with no layering order, our results (Fig. 4*b*) reproduce the peak profiles given by Warren's (1941) solution, including the asymmetric tailing. However, we also find that simulated diffraction from randomly oriented graphitic layer stacks containing one or more *AB*-layer pairs results in (002) reflections that are stronger than the $\{hk0\}$ and $\{h00\}$ in-plane reflections. The lack of such (002) reflections in the core scattering profiles thus leads us to conclude that the interplanar spacings between individual graphene sheets are randomized so extensively that coherent interplanar reflections are difficult to detect. This is nonetheless curious, since one might expect that some fraction of the sheets would accidentally stack in groups of parallel layers with a nearly constant spacing. A possible explanation for the apparent absence of layering order could be that the graphene sheets have variable degrees of curvature and wrinkles due to in-plane disorder, such as occasional replacement of hexagons in the graphene sheets by pentagons and heptagons (e.g., Kroto et al. 1985).

These observations suggest that the aromatic sheet material in the cores resembles clusters of polycyclic aromatic hydrocarbons (PAHs). PAH molecules consist of planar networks of hexagonal carbon rings (having 10 to several hundred C atoms, and diameters typically less than 1 nm) terminated at the periphery by hydrogen atoms. In the limit of large numbers of carbon atoms, the H/C ratio becomes vanishingly small and the structure becomes that of graphene. PAHs have been frequently invoked to explain certain circumstellar infrared emission features, and a plausible case has been made for their origin as condensates in C-rich stellar outflows (Frenklach & Feigelson 1989; Allamandola, Tielens, & Barker 1989; Cherchneff, Barker, & Tielens 1992). Although it is not possible to measure the PAH content of circumstellar graphite directly by TEM analyses, it is worth noting that isotopically anomalous low molecular weight PAHs have been detected in laser desorption/laser ionization mass spectrometry of circumstellar graphite (Messenger et al. 1994).

Another means of characterizing the spherule core material is by the size of its constituent particles. This is accomplished through the Scherrer formula, which relates the observed electron diffraction peak width (FWHM) to the inverse of the particle size. The particular form of the Scherrer formula for the present case of a two-dimensional lattice is derivable from Warren's (1941) analysis as $D = 1.84\lambda/(2\,\Delta\theta)$, where D is the mass-weighted mean particle diameter, λ is the wavelength of the primary electrons (0.0025 nm for 200 keV electrons), and $2\,\Delta\theta$ is the angular FWHM of a diffraction peak. The FWHMs of diffraction-peak profiles for the circumstellar spherule cores, such as the one shown in Figure 4*a*, lie in the range $(1.2\text{–}1.5) \times 10^{-3}$ radians (corrected for instrumental broadening), indicating particle diameters in the range 3–4 nm.

We next compare the electron diffraction profiles for the circumstellar graphite cores (Fig. 4*a*) with the results of a numerical simulation of electron diffraction from a collection of randomly oriented graphene sheets in the size range derived above. Figure 4*b* displays the simulation results for 4 nm graphene, after taking the logarithm of the calculated distribution of scattered intensity (to simulate the response of the TEM negatives that record the diffraction patterns) and after removing the diffuse scattering background. To facilitate direct comparison with the TEM measurements, Figure 4*c* shows the profile after convolution of the numerical results with a Lorentzian function representing the instrumental broadening. Comparison of Figures 4*a* and 4*c* shows that the graphene simulation is reasonably successful in duplicating the peak positions, relative intensities, FWHMs, and (asymmetrical) shapes of the TEM diffraction peaks. Simulations for mean crystallite sizes less than 3 nm give FWHMs that are too broad to be consistent with the measurements. Because of the effect of instrumental broadening, the measured diffraction-peak FWHMs become progressively insensitive to larger crystallite sizes, so that the derived 3–4 nm mean crystallite size is perhaps best regarded as a lower limit to the true mass-weighted mean size.

One important difference between the 3–4 nm simulation peak profiles and the TEM measurements is that the leading edges of the measured peaks rise less sharply than those in the simulations. This is apparently because in the simulation a fixed crystallite size was assumed, and not a *distribution* of sizes that undoubtedly characterizes the real situation. Larger crystallites tend to dominate the diffraction peaks (and largely determine their FWHMs) because the coherently scattered intensity from a graphene sheet is proportional to the square of its mass. Smaller crystallites affect the diffuse scattering background and mainly tend to broaden the base of the peak profile (cf. Klug & Alexander 1962). To investigate the effect of nonuniform size on the diffraction profile, we performed numerical simulations of diffraction from bimodal graphene size distributions, taking 4 nm as the size of the larger particles. The results showed that mass fractions of particles roughly 1 nm or less can range up to several tens of percent without significantly

increasing the peak FWHMs beyond the values obtained for 4 nm particles alone. As expected, inclusion of the smaller particles generated diffraction peaks with broader bases that more closely matched those observed (Fig. 4*a*). Comparison of the electron diffraction data with simulations thus indicates that while the bulk of the mass in circumstellar graphite cores is in graphene sheets several nanometers in size, large numbers of particles ≤ 1 nm may also be present.

For direct comparison with material in the PAH size range, we performed SAD analyses of samples of the very large PAH dicoronene ($C_{48}H_{20}$; $\sim 0.7 \times 2$ nm), a network of 48 C atoms that has a molecular weight of 596 g mol^{-1}. The electron diffraction profile and structure of dicoronene are shown in Figure 4*d*. Applying the Scherrer size analysis to dicoronene yields a mean crystallite size of 1.5–1.8 nm, consistent with the actual structural dimensions. Qualitatively, a comparison of Figures 4*d* and 4*a* shows that even this very large PAH is smaller than the average circumstellar graphite core crystallite. As another standard, we analyzed ordinary "amorphous carbon" (a-C), which has islands of structural order with dimensions typically in the range 1.5–2 nm (Robertson & O'Reilly 1987). Comparison of the widths of peaks in the a-C diffraction profile (Fig. 4*e*) with those of Figure 4*a* indicates that the mean crystallite size is larger in the circumstellar graphite cores than in ordinary amorphous carbon.

Thus, the overall conclusion from the electron diffraction analyses is that most of the mass in circumstellar graphite cores is contained in graphene sheets considerably larger (at least 3–4 nm) than typical PAHs, with each sheet containing several hundred C atoms, although as much as one-quarter of the mass may be in smaller particles ($\lesssim 1$ nm), conceivably PAHs. This further implies that the smaller particles in the cores must be many times more numerous than the larger ones.

3.2. *Electron Energy Loss Spectrometry*

Another means of characterizing carbonaceous material is electron energy loss spectrometry (EELS), particularly through loss mechanisms involving small energy transfer. Fast electrons traversing matter can lose energy by setting up collective valence electron oscillations in the target material. The quantum of this oscillation is the plasmon, whose energy scales with the square root of valence electron number density and is generally in the range of a few tens of electron volts. The plasmon energy is sensitive to composition and structural details, and in the particular case of carbon and its compounds depends upon density and H content (cf. Bernatowicz, Gibbons, & Lewis 1990). The diamond plasmon energy (33.5 eV; $\rho = 3.52$ g cm^{-3}) is thus greater than that of graphite (26–27 eV; $\rho = 2.25$ g cm^{-3}), which is in turn greater than that for amorphous carbon (a-C) ($\sim$24–25 eV; $\rho \sim 2$ g cm^{-3}). Addition of H, as in hydrogenated (a-C:H) amorphous carbon (or PAHs), lowers both the matter density and the valence electron number density, leading to further decreases in plasmon energy (22–24 eV, $\rho = 1.4$–1.8 g cm^{-3}; Robertson 1986).

In Figure 5 we compare our measurements of plasmon peak energies for the circumstellar graphite cores, vapor-deposited black amorphous carbon (a-C), graphite, and the PAH dicoronene. The plasmon energy for graphite depends upon its orientation with respect to the electron beam, being larger ($\sim$27 eV) when the beam is parallel to the unique ("c") crystallographic axis and smaller ($\sim$26 eV) when perpendicular to it (i.e., parallel to the layering). It is clear from Figure 5 that plasmon energies for the cores (26.1 eV) are markedly greater than those for dicoronene (23.5 eV) and a-C (24.5 eV). Thus, we are again led to the conclusion that PAHs cannot constitute the major mass of the circumstellar graphite cores. To get a quantitative estimate of the fraction of the core material that could be present in the form of PAHs, we modeled the cores as mixtures of graphitic carbon and dicoronene, using the property that the plasmon energy of a binary mixture is intermediate to the plasmon energies of the two constituents, depending quasi-linearly on the fraction of each (see Joy 1986). Choosing a mean value for the graphite (26.6 eV), we found that large PAHs such as dicoronene could constitute 5%–25% of the core mass, a range compatible with the results of the electron diffraction analyses discussed above.

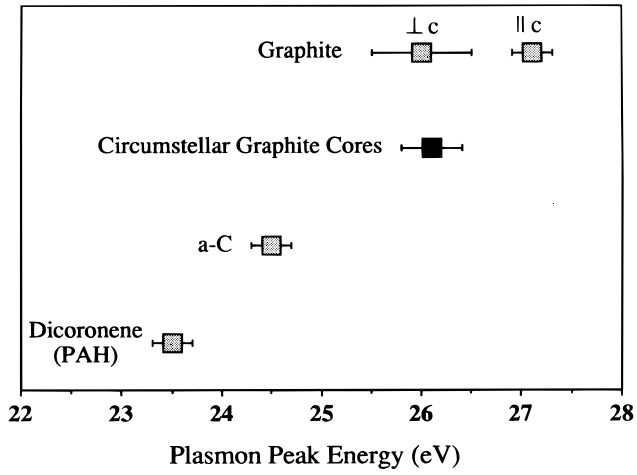

FIG. 5.—Peak plasmon energies from low energy loss in electron scattering, for circumstellar graphite core material, compared with plasmon energies measured for graphite (perpendicular and parallel to the c crystallographic stacking direction), vapor-deposited black amorphous carbon (a-C), and the polycyclic aromatic hydrocarbon (PAH) dicoronene.

Taken at face value, the plasmon energy of the core material implies that its density is greater than that of vapor-deposited a-C, and only marginally less than that of graphite. But electron diffraction shows that the cores are aggregates of randomly oriented graphene sheets, so it is fair to ask whether the plasmon energy could simply reflect the surface electron density of these sheets, even though the bulk density of the core material may be low. We think that a low-density packing of single graphene layers is not a suitable model, for two reasons. First, surface plasmons couple in very thin films to form two modes: the energy of one of them approaches the bulk plasmon energy as film thickness decreases, while the other drops to lower energy. One must ask, therefore, if the observed core plasmon might be the high-energy surface plasmon mode of a graphene sheet. The answer is no; theory (Raether 1965) and experiment (Boersch et al. 1966; Swan, Otto & Fellenzer 1967) agree that the probability of exciting the low-energy mode with an electron beam is roughly independent of film thickness, while the probability of exciting the high-energy mode decreases rapidly with decreasing film thickness.

Thus, the 26 eV core plasmon energy can only be explained by a near-graphitic bulk density of carbon atoms, even though layer-layer correlation in the core structure is

not apparent from electron diffraction analysis. Second, the cores appear to be dense in electron images made under diffraction contrast conditions (e.g., see Fig. 7*c*). If the cores consisted of widely separated graphene layers, they would appear to be lighter in the images presented here, rather than the medium gray shown. However, it is impossible to generate a near-graphitic bulk density by packing that only involves the randomly oriented ~ 4 nm graphene sheets that constitute most of the mass of the core material. The EELS results therefore also imply the existence of large numbers of smaller ($\lesssim 1$ nm) structural units to act as "space fillers," in agreement with the inference based on the shape of diffraction profiles alone (§ 3.1).

In summary: TEM analyses indicate that the graphite spherules consist of shells of well-graphitized carbon often surrounding cores of nanocrystalline carbon. Most of the core material mass resides in 3–4 nm diameter graphene sheets, but as much as one-quarter of the mass is contributed by many times more numerous $\lesssim 1$ nm particles, conceivably PAHs.

4. FORMATION OF CIRCUMSTELLAR GRAPHITE SPHERULES

Having characterized the carbon structures within the circumstellar graphite, we next consider the formation of the spherules themselves, starting with the conditions responsible for the production of the nanocrystalline cores. As described above, TEM analyses reveal that the nanocrystalline cores consist of small ($\lesssim 4$ nm) graphene sheets with little, if any, collective three-dimensional crystallographic order. It appears possible to understand the formation of the cores in terms of a generalization of the model proposed by Allamandola et al. (1989) to account for the formation of "soot" in C-rich stellar atmospheres by aggregation of PAH molecules. These authors pointed out that maximum stability geometrical configurations (calculated by Miller, Mallard, & Smyth 1984) for PAH molecule pairs naturally lead to an amorphous structure for the soot particles.

To account similarly for the TEM observations of the core material (§ 3) by aggregation of graphenes, the mechanism of growth of graphenes should result in a distribution of sizes prior to their aggregation, with smaller particles outnumbering larger ones by a large factor, and the development of graphitic stacking order should be inhibited. The former condition is reasonable, assuming that the growth of the graphene simply represents the end stages in the gas-phase reaction chains that build larger PAHs from smaller ones (cf. Keller 1987). The latter condition is likely to be fulfilled, as long as the adsorption energies for carbon-bearing gas species on the graphene surface are not too large (cf. Omont 1986). The mean sticking time τ_s for an adsorbed molecule will be of order $(1/\nu_0)\ \exp\ (\varepsilon/kT)$ (cf. Podosek, Bernatowicz, & Kramer 1981). For an escape attempt frequency ν_0 of the adsorbed species of $\sim 10^{12}$–10^{13} s^{-1} and an adsorption energy $\varepsilon \lesssim 1$ eV, the mean sticking time τ_s is $\lesssim 1$ ns at a carbon condensation temperature of $T = 1650$ K (§ 6.1). Comparing this timescale to the arrival frequency of condensable carbon-bearing species on a given condensation site at moderate pressures (several minutes at $P = 1$ dyne cm^{-2}) shows that growth of a new graphene layer on top of a preexisting one is unlikely, particularly when more strongly bonding sites such as the edges of the sheets are available. For bond energies as large as those among carbon atoms at a graphene sheet edge (6–7 eV), the lifetime against thermal desorption is many years at any plausible condensation temperature, so lateral growth of graphene sheets is overwhelmingly favored, particularly if adsorbed atoms are able to migrate over the surface at thermal speeds ($\sim 10^5$ cm s^{-1}) and find a strongly bonding sheet edge before they are desorbed.

Given the likely possibility that the nanocrystalline cores are formed by coagulation of graphenes, we then need to account for the structural transition to the surrounding layers of graphitic carbon that are observed in the TEM. There are only two explanations for the core-rim structure: either graphite rims formed by alteration of the core material, or the rims were deposited on the cores. Considering an alteration origin first, we note that the most common means of transforming "amorphous" carbon into graphite is to raise the temperature sufficiently to produce extensive structural reorganization, including growth of aromatic units and elimination of heteroatoms and defects (cf. Marchand 1987). Shock propagation in circumstellar atmospheres can lead to temperature increases in the stellar outflow (e.g., Bowen 1988), and possibly to thermal alteration of preexisting grains. Thermal annealing of carbonaceous grains has indeed been proposed to account for UV circumstellar extinction spectra of C-rich stars (Blanco, Fonti, & Orofino 1995). However, in particles as small as our circumstellar graphite spherules, it would be difficult to only heat and graphitize the exterior without changing the core. For any reasonable thermal conductivity, it is certain that graphitization of the spherule exterior due to heating would be accompanied by near-simultaneous interior graphitization.

Another mechanism for altering grain surfaces is energetic particle irradiation. It has been shown, for example, that intense irradiation of amorphous C by energetic (hundreds of keV) electrons can result in extensive graphitization (Ugarte 1992). However, if the flux of particles is sufficiently high, as in this case, we are once again in the regime of surface heating and the above discussion applies. Experiments have shown that bombardment of amorphous carbon by energetic ions (for which electronic stopping is the dominant energy loss mechanism) can lead to measurable increases in electrical conductivity, reflecting the growth of graphitic domains (Döbeli et al. 1991; Dresselhaus & Kalish 1992), but the size of these domains is generally less than 1 nm. We know of no data that suggest that energetic particle bombardment can produce graphitic regions with the sort of extended crystallographic continuity that we observe in the shells of circumstellar graphite (hundreds of nanometers), except in cases of high incident flux where significant sample heating is involved.

We are therefore left with the second hypothesis, that the graphitic rims were added to the cores by vapor deposition. Nanocrystalline cores are *always* surrounded by well-graphitized carbon, never the reverse situation; nor are there any cases in which the two forms of carbonaceous matter occur in alternating layers. This suggests that the sequential changes in the internal structure and composition of the circumstellar graphites correspond to monotonically changing conditions, such as a progressive decrease in the partial pressures of carbon-bearing vapor species. For graphite to condense from a vapor, the C/O ratio in the vapor phase must exceed unity (cf. Larimer 1975). If this is the case, part of the carbon in the vapor phase will pair up with the available oxygen in tightly bound CO molecules,

which, however, will remain uncondensed in the temperature range of interest here (cf. § 6.1). Only the excess carbon, which will be present mainly in the condensable form C_2H_2, will be available to form graphite.

In considering the possible effect of variation in the partial pressure of this condensable carbon, it is important to note that refractory carbide grains often served as heterogeneous nucleation sites for carbon condensation, as inferred from their occurrence in the centers of about half of the spherules in which such carbide grains are found (cf. § 5). These central carbide grains are *always* surrounded by mantles of well-ordered graphite that could only have originated by vapor deposition. A possible explanation for this observation is that the presence of previously formed carbide crystals may have initiated graphite condensation at relatively low degrees of condensable carbon supersaturation, leading to slow growth of graphite with a high degree of crystallinity. As we indicated above, however, lateral growth on the edges of graphene sheets is overwhelmingly favored during vapor growth, whereas direct addition of new layers is difficult owing to the short lifetime of adsorbed molecules on the graphene surface. Therefore, the growth of graphite mantles on the carbide seeds probably occurred in a manner similar to the "icospiral" growth mechanism proposed by Kroto and his coworkers (Kroto et al. 1985). According to this idea, once a small aromatic network of carbon atoms has been established on the carbide surface, atoms are permanently added only to the graphene sheet edge, with the growing sheet of atoms continuously advancing over itself, analogous to the growth of a nautilus.

The corresponding inference is that the nanocrystalline cores formed in cases where few refractory grains were available to serve as heterogeneous nucleation centers, so that carbon condensation was delayed until homogeneous nucleation could occur at higher supersaturation levels. We speculate that the ensuing rapid condensation resulted in the formation of isolated aromatic networks (PAHs and graphene sheets) in the gas that subsequently coalesced to form the nanocrystalline cores. This is consistent with the conclusion based on TEM analyses (§ 3), that the cores are mixtures in which small particles are far more numerous than larger ones, because nucleation rates outstrip growth rates under conditions of high supersaturation.

In accord with the notion that a higher degree of crystallinity results if the rate of surface migration of condensed species is fast relative to the rate of new arrivals, we presume that reduced carbon partial pressure favors deposition of carbon with long-range order (i.e., graphite) on the nanocrystalline cores. Thus, after the cores formed, the local gas-phase number density of condensable carbon may have become significantly reduced, favoring the deposition of graphite on these cores by the same "icospiral" mechanism that we have invoked for the case of graphite deposition on carbides.

We note that Cadwell et al. (1994) had predicted that refractory grains could serve as nuclei for high-temperature carbon condensation in stellar atmospheres, and that the deposited material would likely be present in the form of aromatic networks, consistent with our observations of carbide grains mantled by well-graphitized carbon. They speculated that the species serving in this role would be SiC. However, as we discuss below (§ 5), SiC is generally not observed in the spherules (nor is it expected to condense prior to graphite on the basis of equilibrium thermodynamics [§ 6.1]); rather, the nuclei that we do observe are carbides of Ti, Mo, and Zr.

The internal geometry of circumstellar graphite spherules also suggests that the physical conditions under which they formed did not, in general, differ radically from one stellar environment to another. Figure 6*a* is a histogram of apparent rim thicknesses observed in ultrathin sections of the graphite spherules. Because a given section may not contain the spherule center, some of the apparent rim thicknesses are probably displaced to values somewhat greater than in the actual distribution; nonetheless, the measured distribution is sharply peaked, with three-fourths of the spherules having apparent rim thicknesses in the range 0.1–0.4 μm. In Figure 6*b* we display the relation of apparent rim thickness to apparent radius for individual spherule sections; here again we must bear in mind that the data may be displaced from their true values by varying amounts (to the left and up in the plot) due to the effects of sectioning. Although spherules with radii greater than ~ 1 μm tend to have thicker rims, the smaller spherules display little evidence of a relation between size and rim thickness: the majority fall within the narrow range noted above. The general lack of correlation between spherule size and rim thickness is not unexpected if, as we have argued above, the graphitic rims

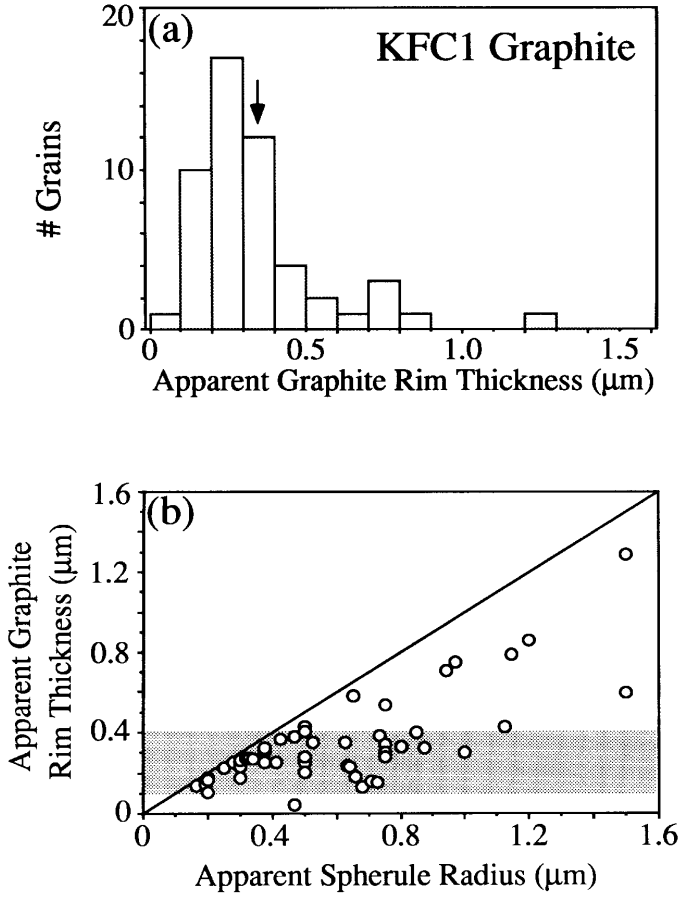

FIG. 6.—(*a*) Histogram of apparent graphitic outer shell (rim) thicknesses measured in ultrathin sections of circumstellar graphite spherules. The arrow denotes the mean thickness. (*b*) Apparent rim thickness vs. apparent graphite spherule radius. All data plot below the diagonal line, because the rim thickness cannot exceed the particle radius. Seventy-five percent of the spherules have rim thicknesses from 0.1 to 0.4 nm (*shaded area*), and there is no apparent correlation of rim thickness with grain size for spherules with rim thicknesses in this range.

originated by vapor accretion. The reason is that when a particle grows by capturing a specific gaseous species on its surface, the accreted thickness depends directly on the number density of that species in the gas and the deposition time, but not on the particle size. Assuming that the rims formed by vapor accretion, the relatively narrow range of rim thickness for the smaller graphites may be taken as evidence that the number density of carbon available for rim deposition, as well as the deposition times, did not vary widely in the various stellar atmospheres in which these graphite spherules formed. However, other considerations (§ 7.2) suggest that the largest grains (radii $\gtrsim 1$ μm) require significantly higher carbon number densities and/or longer deposition times for their formation.

5. INTERNAL CRYSTALS IN CIRCUMSTELLAR GRAPHITE

We detected crystalline metal carbide inclusions in approximately one-third of the spherules studied. Carbide inclusions are undoubtedly more common than this because only one section from any spherule was studied. The geometrical mean size of the crystals ranged from ~ 5 to ~ 220 nm, with three-quarters of them in the range ~ 5 to ~ 30 nm (Table 1).

Energy dispersive X-ray (EDS) analysis of the crystals indicates that they are generally carbides of the refractory elements Ti, Zr, and Mo, although some crystals rich in Ni, Ru, or Fe were also detected. The compositions of crystals for which quantitative EDS chemical analysis was performed are given in Table 1 as atomic ratios relative to the (generally dominant) element Ti. The variability in the ratios points to a significant degree of solid solution among these elements. Crystals range from "pure" Ti carbide (with no other elements detected, e.g., B1p1) up to Zr carbide with only 5 atom% Ti (e.g., B3b2). In some cases electron diffraction patterns for individual crystals rich in Ti indicated *d* spacings commensurate with those of cubic TiC (cf. Bernatowicz et al. 1991). In many cases, however, reliable or diagnostic spacings could not be obtained, and the identification of the included crystals as carbides is based on the EDS detection of metal elements unaccompanied by significant amounts of anions other than carbon (specifically oxygen, nitrogen, or sulfur).

Crystals included in the spherules occur in both the nanocrystalline core material and the graphitic mantles. As we noted in § 4, sometimes the refractory carbides are located in the centers of the spherules. Central crystals are usually euhedral (i.e., having sharp planar boundaries) and solitary (Fig. 7*a* [Pl. 18]), but sometimes they occur in clusters (Fig. 7*b*). Noncentral internal crystals were also observed (Fig. 7*c*), and in many cases more than one was

TABLE 1

ELEMENTAL RATIOS FOR KFC1 GRAPHITE INTERNAL GRAINS[a]

Grain[b]	Size[c] (nm)	Cr/Ti	Fe/Ti	Ni/Ti	Zr/Ti	Mo/Ti	Ru/Ti
B0g1	40–60	0.01 ± 0.002	0.003 ± 0.001	...	0.12 ± 0.006	0.05 ± 0.006	...
B0g4	10	0.05 ± 0.03	0.06 ± 0.02	...	0.85 ± 0.01	0.37 ± 0.08	...
B0q1	10–25	0.12 ± 0.11	1.4 ± 0.2	0.15 ± 0.07	4.1 ± 0.4	0.53 ± 0.19	...
B0q2	10–20	0.06 ± 0.02	0.08 ± 0.02	...	0.47 ± 0.06	0.30 ± 0.10	...
B1a1	25–35	0.03 ± 0.01	0.03 ± 0.01	...	0.28 ± 0.04	0.22 ± 0.05	...
B1a2	3–25	0.33 ± 0.31	0.86 ± 0.43	1.6 ± 0.6	7.0 ± 2.7	1.7 ± 1.1	...
B1a3	15	...	0.30 ± 0.13	0.45 ± 0.14	0.41 ± 0.13	0.54 ± 0.14	...
B1a4	10	0.54 ± 0.56	...	1.4 ± 0.9	15.9 ± 8.8	3.4 ± 3.3	...
B1d	5	0.80 ± 0.35	0.32 ± 0.19	...	12.8 ± 2.6	2.6 ± 1.0	...
B1f	10	1.7 ± 1.1	0.66 ± 0.54	...	10.8 ± 7.2	3.6 ± 2.8	...
B1g	40–70	0.03 ± 0.005	0.01 ± 0.004	...	0.012 ± 0.007	0.017 ± 0.008	...
B1k	10	...	0.07 ± 0.04	...	...	...	...
B1p1[d]	10	...	...	...	...	...	...
B1p2	10	...	0.57 ± 0.31	...	3.2 ± 0.3	1.0 ± 0.8	...
B1t	10–20	0.29 ± 0.18	...	...	12.6 ± 1.6	2.3 ± 0.5	...
B1u1	20	0.03 ± 0.01	0.26 ± 0.03	0.06 ± 0.02	1.8 ± 0.2	0.36 ± 0.12	0.51 ± 0.08
B1u2	10	0.57 ± 0.25	...	...	6.6 ± 1.7	1.7 ± 0.7	...
B1u3	6	...	0.35 ± 0.25	...	0.74 ± 0.55	2.0 ± 1.0	...
B1u5	10	0.14 ± 0.07	0.21 ± 0.08	...	0.76 ± 0.40	0.67 ± 0.22	...
B1w1	30–40	0.05 ± 0.008	0.41 ± 0.01	0.09 ± 0.01	0.087 ± 0.020	0.048 ± 0.021	0.18 ± 0.01
B1w2	12	0.02 ± 0.02	0.10 ± 0.05	0.07 ± 0.02	0.15 ± 0.10	0.22 ± 0.12	0.065 ± 0.054
B1w3	10	...	0.87 ± 0.15	0.58 ± 0.13	0.15 ± 0.13	0.41 ± 0.15	1.16 ± 0.17
B1aa1	30	0.16 ± 0.11	0.23 ± 0.13	...	4.8 ± 0.7	0.35 ± 0.34	...
B1aa2	10	...	1.28 ± 0.20	...	4.7 ± 0.9	0.72 ± 0.50	...
B1ac	20	0.01 ± 0.007	...	...	0.073 ± 0.020	0.21 ± 0.02	...
B1ad	125	0.025 ± 0.009	0.01 ± 0.01	...	...	...	...
B2e	5	0.39 ± 0.10	0.24 ± 0.10	...	1.3 ± 0.3	0.68 ± 0.22	...
B2f	30–50	0.02 ± 0.006	0.02 ± 0.007	...	...	...	...
B2k	75–120	5.6 ± 0.6	19.3 ± 2.0	0.15 ± 0.10	0.41 ± 0.16	0.35 ± 0.18	...
B3b1	220	0.008 ± 0.001	0.002 ± 0.0006	...	0.034 ± 0.003	0.009 ± 0.003	...
B3b2	85–100	0.09 ± 0.06	0.06 ± 0.03	...	18.9 ± 0.9	1.4 ± 0.1	...

[a] Atomic ratios. Stated uncertainties are for 1 σ precision and reflect counting statistics and background subtraction only. The accuracy of reported ratios is ±15%. The absence of a numerical entry indicates that the element was not detected. The table does not include entries for cases where internal grains were detected but elemental concentrations could not be obtained.

[b] Graphite spherule designations are shown in boldface type; for spherules having more than one internal crystal with a measurable elemental composition, each crystal is designated with a numeric index, and its composition is tabulated in a separate row.

[c] Minimum-maximum projected crystal dimensions determined from TEM micrographs. Single entries are for roughly equidimensional grains.

[d] Only Ti was detected.

detected within a given spherule (Fig. 7*d*). Simple probability considerations show that an apparent central location of crystals is not likely to be an artifact of the projected nature of TEM images. We calculate a less than 1% probability that a crystal in an arbitrary location within a spherule will appear to be in the center of a random section through it, whereas we find crystals to be centrally located in roughly half of the spherule sections that have internal crystals. Whether central crystals occur singly or in clusters, there can be little doubt that they formed *before* extensive carbon condensation occurred and that they served as sites for this condensation.

We choose from Table 1 three spherules that have three or more internal crystals, and we display their elemental ratios (normalized to solar values) in Figure 8. All of the crystals have atomic Cr/Ti and Fe/Ti ratios 1–3 orders of magnitude smaller than the solar values. On the other hand, Zr/Ti, Mo/Ti and (in two spherules) Ru/Ti ratios are enhanced by factors of 10 to several thousand. The large variability in elemental ratios among internal crystals within a given spherule precludes the possibility that these crystals could have exsolved from their respective spherules, or that they could have formed as the result of inward diffusion of metal elements after carbon condensation. The simplest explanation for these observations is that the non-central crystals also formed prior to carbon condensation and were subsequently occluded during the growth of carbon spherules.

Enrichments of Zr and Mo, by factors of 10–100, are predicted to occur in the envelopes of AGB stars through *s*-process nucleosynthesis in their He-burning shells (R. Gallino 1994, private communication). Such enrichments are indeed astronomically observed in N-type carbon stars, which have *s*-process enrichments of Zr by factors of 10–100 relative to Ti (Gustafsson 1989). However, *s*-process enrichment *alone* is incapable of accounting for the elemental compositions of the internal crystals. First, there are large variations in elemental ratios from crystal to crystal in the *same* graphite spherule; second, the Zr and Mo enrichments relative to Ti are sometimes more than an order of magnitude greater than those predicted for AGB stars and observed in stellar atmospheres. The Zr and Mo enrichments in the crystals must therefore be due in part to elemental fractionation accompanying condensation of carbides, as discussed in § 6.

Figure 9 compares solar-normalized Mo/Ti ratios to Zr/Ti ratios in the internal crystals for those spherules listed in Table 1 for which all three elements were detected. In all of these cases Mo/Ti and Zr/Ti ratios are dramatically elevated relative to the solar ratios, by 1 to more than 3 orders of magnitude. Here again we observe that the elemental

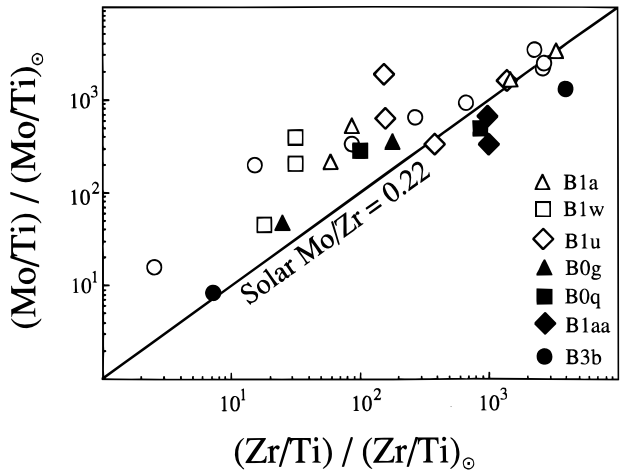

FIG. 9.—Comparison of Mo/Ti and Zr/Ti ratios (normalized to solar abundances) in carbide crystals within circumstellar graphite spherules that have measurable abundances of all three elements. Error bars have been suppressed for clarity (cf. Fig. 11 and Table 1). Only spherules having more than one crystal are listed in the legend; if only one crystal was measurable within a spherule, its composition is shown as an open circle. Solar composition plots in the lower left-hand corner, and the diagonal line is the locus of solar Mo/Zr ratios. The variations in elemental composition among crystals from individual spherules, and the substantial enrichments of Mo and Zr relative to Ti, point to chemical fractionation accompanying condensation of these crystals.

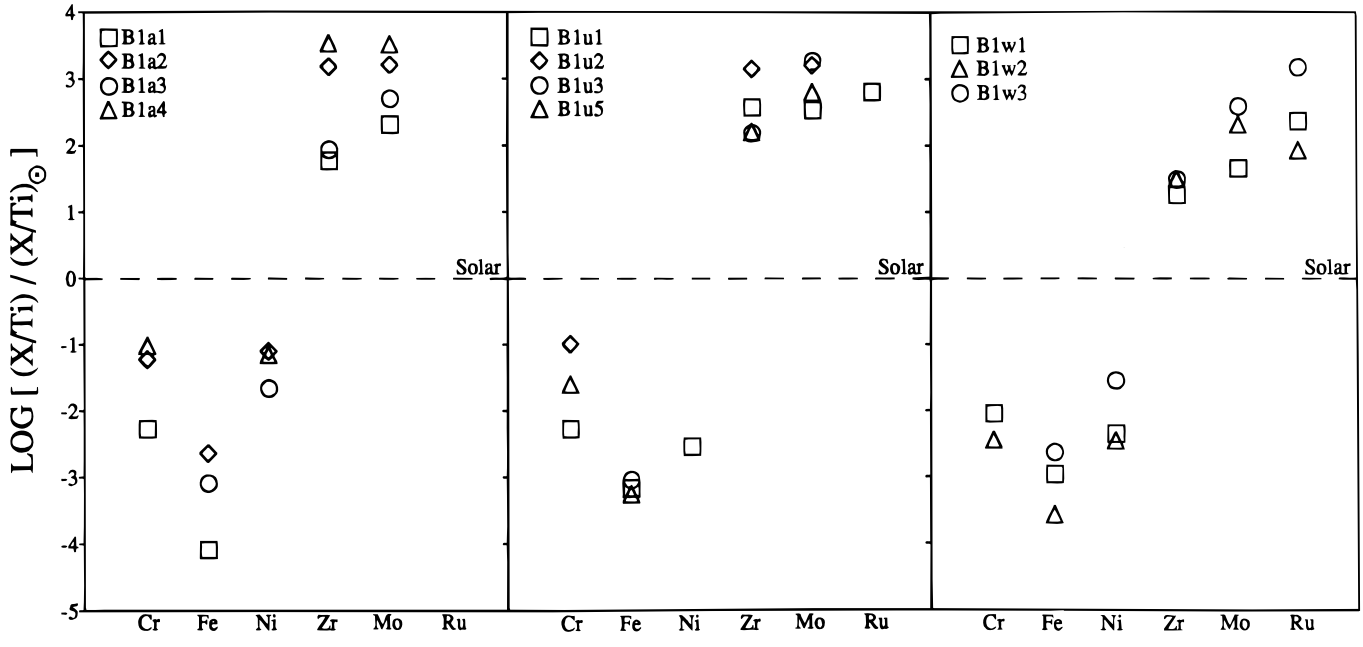

FIG. 8.—Atomic abundances (relative to Ti) of elements in carbide crystals from three circumstellar graphite spherules, normalized to solar ratios (cf. Table 1). Note the several-order-of-magnitude enrichments of Zr, Mo, and Ru.

ratios vary widely among crystals within a given spherule. The more refractory crystals (e.g., those with Zr/Ti more than 500 times solar) have Mo/Zr ratios less than or equal to the solar value of 0.22 (Anders & Grevesse 1989), while in less refractory ones Mo is enriched relative to Zr as well as Ti. These trends are most naturally explained under the assumption that ZrC condensed first, followed by MoC (or Mo_2C) and TiC, a conclusion that is consistent with the relative condensation temperatures of these carbides (cf. § 6.2).

It thus appears that carbides (and solid solutions of carbides) were the first-formed minerals, and that the order of their appearance was dictated by the relative condensation temperatures of various carbide species. In some cases these preexisting carbides acted as heterogeneous nuclei for subsequent carbon condensation. In other cases the preexisting carbides collided with and stuck to growing carbonaceous spherules and were entrained in them as carbon condensation proceeded. The condensation sequence of refractory carbides followed by graphite puts fairly tight constraints on the permissible stellar atmosphere C/O ratios, because, under reasonable pressures, C/O ratios a few tens of percent greater than unity or more inevitably lead to condensation of graphite prior to refractory carbides (§ 6.1).

It is noteworthy that SiC is *not* generally observed in the spherules, despite the fact that the cosmic abundance of Si is far greater than that of the other metal elements that occur in carbides within circumstellar graphite. SiC is known to be present in carbon-rich stellar ejecta (e.g., Whittet, Duley, & Martin 1990) and micron-sized, isotopically anomalous circumstellar SiC crystals have been found in many types of primitive meteorites (cf. Bernatowicz et al. 1987; Anders & Zinner 1993). Of the 67 spherules studied, however, only one contained crystals of SiC. This observation can also be explained on the basis of relative condensation sequence. Because of the low abundance of Ti relative to C, the condensation of TiC does not significantly deplete the gas of carbon. However, Sharp & Wasserburg (1995) point out that for C/O in the astronomically observed range for carbon stars, the amount of condensable C remaining in the gas by the start of SiC formation is usually much less than the amount of gaseous Si, so that SiC must largely be produced by reaction of Si gas with preexisting graphite. Much of the condensable carbon has already been used up, so there is little graphite condensation at the time of SiC formation, and therefore little opportunity for SiC grains to be enclosed by graphite (cf. § 6.1). The formation of SiC by the reaction of previously formed graphite with Si gas may also help to explain why the presolar SiC from AGB stars found in meteorites is more abundant than the graphite from this source (by a factor of more than 6 by mass in the Murchison meteorite; cf. § 7.4). As Sharp & Wasserburg (1995) point out, a substantial fraction of the graphite inventory must usually react with Si gas to form SiC, so we expect that more SiC than graphite would ultimately result from condensation in AGB atmospheres.

Fegley (1982) and Lodders & Fegley (1993) predicted the formation of the minor element refractory carbides ZrC and MoC on the basis of equilibrium condensation theory. Other predicted refractory condensates such as HfC, NbC, TaC, and WC have not been observed; however, this may be a kinetic effect due to the scarcity of these metal elements, since their solar abundances are lower (up to 2 orders of magnitude) than those of Zr and Mo. They may never have formed as initial condensates because the elements in question are simply too scarce to permit growth before condensation of other carbides. If so, they may be present in solid solution with the more abundant carbides, but below our detection limits. $VC_{0.88}$ is a less refractory condensate that does not suffer from this abundance problem, but we are unable to detect V by EDS analysis in the presence of Ti because of interference from the Ti Kβ peak. It is likely that $VC_{0.88}$, if present, is in solid solution with TiC, because V is generally well correlated with Ti in circumstellar SiC (Amari et al. 1995a).

The observations of carbides enclosed by carbon point to grain condensation from a C-rich gas in stellar outflows (§ 6). Further, because the carbides have been sequestered in protective graphitic mantles since they formed, they must have retained the characteristics of their pristine state during the long period of propagation in the interstellar medium and residence in the solar nebula and in their meteorite parent body. Thus the observational data on their composition and grainsize hold important clues as to the conditions that obtained in the environments of their birth (§§ 6 and 7). They likewise rule out an origin of the spherules in the interstellar medium, because if this were possible, there would be no necessary chemical link between the composition of the refractory grains and the material surrounding them. For example, we might expect to also find refractory oxygen-rich grains (e.g., oxides like corundum, Al_2O_3) mantled by carbon, contrary to observation. An origin in the interstellar medium is likewise rendered improbable by the large range of C isotopic compositions (Fig. 1).

Finally, we turn to a discussion of "atypical" internal crystals that show specific compositional anomalies. The common types of internal crystals are either pure TiC, or mixtures of Ti, Zr, and Mo carbides. The carbides with measurable Zr were *always* found to contain measurable Mo, although in variable proportion. In contrast, Ru accompanies Zr (and Mo) in crystals from only two spherules (in 1 of 4 crystals in B1u, and in all crystals in B1w; see Table 1 and Fig. 8). Since the solar abundance of Ru is only marginally less than that of Mo, this may be a volatility effect, reflecting elemental fractionation accompanying condensation (§ 6.3).

Although in typical internal crystals Fe and Cr are generally much less abundant than Ti (Table 1), we found an atypical Fe-rich central crystal in spherule B2k (Table 1 and Fig. 7*a*). The B2k crystal is large enough ($\sim$100 nm) so that its composition could be measured by EDS analysis in several independent spots (with electron probe size $\sim$20 nm). On one edge of the crystal we detected only Fe and Cr (atomic Cr/Fe = 0.29), while measurements in the interior revealed Ti, Zr, and Mo in addition to Fe and Cr. We take this to mean that the B2k crystal began to form like the more typical ones, with the exception that it was subsequently overgrown by Fe-rich material. We were unable to determine whether this is Fe or Fe carbide, but from the standpoint of position in condensation sequence or condensation temperature it matters little, since these are nearly identical for the two materials (Lewis & Ney 1979). In a gas of solar composition (but with C/O > 1), Fe carbide will condense after both SiC and graphite under plausible astrophysical conditions, so it is difficult to explain not only the condensation of carbon after Fe but also why SiC is not

present in the B2k central crystal. This suggests that the gas phase had nonsolar composition (in particular, a relative enrichment of Fe), and that spherule B2k may have formed in the ejecta of a supernova, after material from deep interior layers mixed with C-rich outer zones (cf. §§ 2.2, 7.4).

6. EQUILIBRIUM THERMODYNAMICS

Equilibrium thermodynamics allows us to infer the relative condensation sequence of graphite and the various carbides observed in the spherules. Calculations by Fegley (1982) had previously shown that refractory carbides such as TiC, ZrC, and MoC form in reducing environments (i.e., at C/O > 1). More recent studies have thoroughly explored the parameter space of pressure, temperature, and C/O ratio (Sharp & Wasserburg 1995; Lodders & Fegley 1993, 1995), so we briefly summarize their results before taking up a discussion of other aspects of the problem.

6.1. *Condensation of Graphite and Pure Carbides*

The types of minerals condensing from a gas with solar abundances of all the elements except C depend critically on the C/O ratio. When C/O < 1, the condensed phases are oxides and silicates. When C/O > 1, most of the oxygen is tied up in CO, allowing graphite and carbides to condense. The latter compositional regime is relevant to the observations reported here. The equilibrium condensation temperatures for graphite and various pure carbides (ZrC, MoC, TiC, SiC) are displayed in Figure 10 as a function of pressure (0.001–100 dynes cm^{-2}) and C/O ratio (1.05–2.0). The graphite condensation temperature is relatively insensitive to pressure, but depends strongly on the C/O ratio; for the carbides the opposite is true. The intersections of condensation curves for graphite and carbides, together with the observational constraints, thus restrict the permissible ranges of C/O and pressure.

For example, at pressures $\lesssim 0.3$ dynes cm^{-2}, TiC condenses after graphite for C/O > 1.05. TEM observations indicate that TiC formed before graphite, however, so pressures larger than ~ 0.3 dynes cm^{-2} are needed for TiC formation. The pressure at which TiC can condense prior to graphite increases as C/O increases, requiring pressures $\gtrsim 1000$ dynes cm^{-2} when C/O $\gtrsim$ 1.5. Such pressures are implausible for grain formation regions in circumstellar atmospheres. Although *photospheric* pressures can approach 1000 dynes cm^{-2}, typical photospheric temperatures (2000–2500 K) are too high for grains to condense. This restricts condensation to regions farther away from the photosphere, where pressures and temperatures are lower. If we thus set $0.1 \lesssim P \lesssim 100$ dynes cm^{-2} as a plausible pressure range, in accord with the limits set by the TEM observations and stellar atmosphere models, the corresponding C/O range is roughly $1.05 \lesssim$ C/O $\lesssim 1.2$ (cf. Sharp & Wasserburg 1995; Lodders & Fegley 1995), consistent with the C/O in carbon stars (Lambert et al. 1986; Olofsson et al. 1993). Within these limits, the approximate ranges in *initial* condensation temperatures are TiC → 1565–1805 K, graphite → 1590–1760 K, and SiC → 1390–1630 K (Lodders & Fegley 1995).

It is important to note that these conclusions depend on the assumption that thermochemical equilibrium is reached in the grain formation environment. However, in regions of circumstellar atmospheres sufficiently far from the stellar

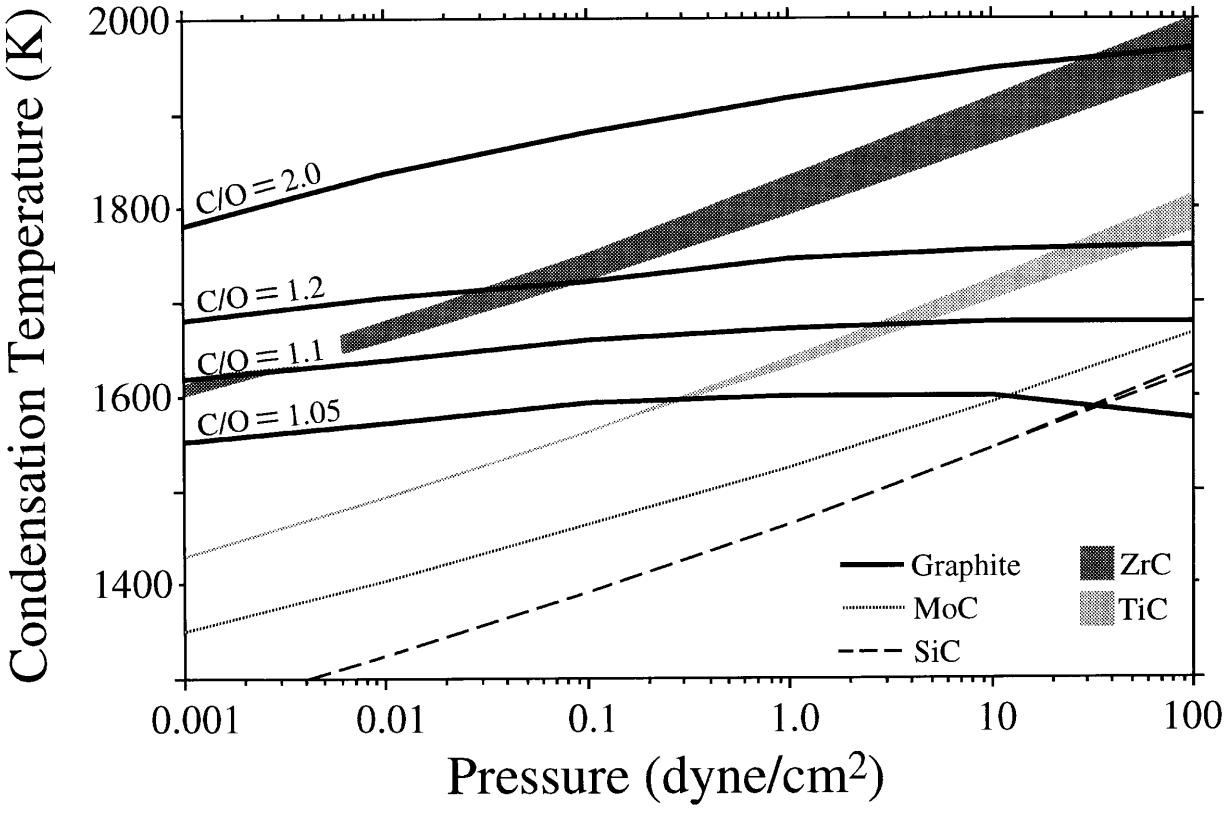

FIG. 10.—Equilibrium condensation temperatures for various carbides and graphites as a function of total pressure and C/O ratio (from 1.05 to 2). Solar abundances were used for all elements except carbon. Condensation temperatures for ZrC, TiC, and SiC vary slightly with C/O and are displayed as envelopes. For these compounds, the lower boundary of the envelope is for C/O = 1.05, and the upper boundary is for C/O ≥ 2.0. For MoC, the condensation temperature does not vary with C/O in the displayed pressure range. The condensation temperature of Mo_2C (not shown) is only a few degrees higher than for MoC at any given pressure. The data are taken from Lodders & Fegley (1995).

photosphere, equilibrium timescales will be longer than characteristic cooling timescales. Mineral assemblages grown at higher temperatures will be "frozen in" as the gas-grain mixture expands and cools, because the slower reaction kinetics cause grains to fall out of equilibrium with the gas. For the present purpose, the key question is whether there is an approach to gas-grain equilibrium sufficiently near the photosphere, where high-temperature condensates may form. The good agreement between observed and calculated trace-element abundance patterns in circumstellar SiC (Amari et al. 1995a; Lodders & Fegley 1995) implies that this is indeed the case. Our TEM observations (§ 5) also largely support this conclusion, since the mineral association of TiC and graphite is what is predicted to form.

Also important is that we do *not* observe SiC grains inside of graphite. According to equilibrium thermodynamics, SiC can form prior to graphite only at relatively high pressures ($\gtrsim 30$ dynes cm^{-2}) for any C/O $\gtrsim 1.05$ (cf. Fig. 10). We therefore do not generally expect SiC to be found within graphite spherules. Our observations confirmed this expectation: only once did we observe SiC within graphite, despite many observations of carbon condensed around other, more refractory carbides (§ 5). Although several authors (e.g., Lewis & Ney 1979; Czyzak, Hirth, & Tabak 1982) have commented on the difficulty of nucleating graphite, and have predicted that its condensation temperature will be substantially depressed below the equilibrium condensation temperature, we see no evidence for this. Our observations indicate that graphite must typically condense prior to SiC formation, consistent with the predictions of equilibrium thermodynamics for astrophysically plausible pressures.

The above discussion applies to a gas with Si, Ti, and other metal elements present in solar proportions. We have not yet discussed Zr and Mo, because they introduce another variable, namely, the extent of *s*-process enrichment. It is true that Si and Ti isotopic compositions can be altered by neutron capture in *s*-process nucleosynthesis, but the overall effect cannot modify their absolute abundances significantly. However, the abundance of dominantly *s*-process elements such as Zr can be enriched above solar proportions by several orders of magnitude. Even for solar proportions, ZrC condenses before graphite and TiC for all C/O ratios and pressures in the ranges inferred above; the condensation temperature of MoC, however, is between that of TiC and SiC (Fig. 10). With *s*-process enrichment, the condensation temperatures of ZrC and MoC increase. For example, with C/O = 1.05 and $P = 10$ dynes cm^{-2}, the condensation temperature of MoC is the same as that of graphite (~ 1600 K) for a solar Mo abundance, but moves up to the condensation temperature of TiC (~ 1700 K) when Mo is increased to 30 times solar (Lodders & Fegley 1995). Because many of the internal crystals in the graphite are not pure phases, but mixtures of Ti-Zr-Mo carbides (§ 5), we next explore the constraints on condensation conditions that may be derived from considering the compositions of these grains.

6.2. *Solid Solution of Refractory Carbides*

From materials science studies (e.g., Samsonov 1974) refractory carbides are known to form solid solutions, and the observation of Zr-Ti-Mo–bearing carbides in the graphites suggests that solid solution determined the compositions of these grains. Here we describe the results of thermochemical equilibrium calculations for grains forming ideal solid solutions of ZrC, TiC, and MoC, using C/O = 1.05 and $P = 1$ dyne cm^{-2} as typical values to illustrate condensation behavior. Details of the computational procedure are described elsewhere (Lodders & Fegley 1993, 1995).

The Zr/Ti and Mo/Ti ratios (cf. Table 1) of the internal carbides in spherules (*filled circles*) are compared with compositions from the solid solution calculations (*curves*) in Figure 11; a line showing the locus of solar Mo/Zr is also indicated. We first consider the composition of grains condensing from a gas with Mo and Zr at solar abundances (curve labeled "Mo, Zr = solar"). When ZrC starts forming (1794 K), very little Ti ($\sim 10^{-4}$% of total Ti) and Mo ($\sim 5 \times 10^{-3}$% of total Mo) can dissolve in ZrC, so the grains are Zr-rich and have high Zr/Ti ratios (~ 200) and Mo/Ti ratios of about 0.04. Further condensation removes more Zr from the gas, and at 1720 K about 90% of all the Zr is condensed as ZrC. Because these grains contain about 0.02% of all Ti and ~ 1% of Mo in solid solution, the Zr/Ti is pushed to lower values (Zr/Ti ~ 25). On the other hand, the Mo/Ti ratio becomes only slightly smaller (~ 0.035), because incorporation of Mo and Ti into ZrC is increasing in similar proportions. Once the temperature drops to about 1630 K, more Ti (4% of total Ti) and Mo (56% of total Mo) are dissolved in ZrC, so the curve bends toward the solar Mo/Zr line. The transition from solid to dashed curve indicates the temperature where about 10% of the total Ti is condensed and a more TiC-rich ZrC-TiC "alloy"

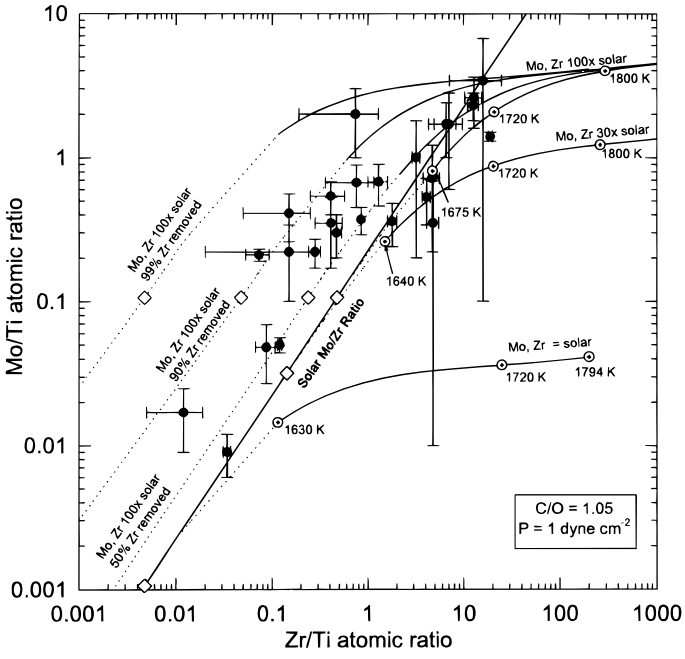

FIG. 11.—Measured Mo/Ti and Zr/Ti atomic ratios in carbides from circumstellar graphite (data from Table 1) compared with calculated condensation tracks for ideal solid solutions (*curves*). The curves are labeled "solar," "30 × solar" and "100 × solar" to indicate overall Mo and Zr abundances used in the calculations. Curves for some percentage removal of Zr (50%, 90%, 99%) are also shown for the 100 × solar case. Condensation starts out with the formation of Zr-rich grains (*solid curves*). The switch from solid to dotted curves occurs where ~ 10% of total Ti is condensed. Dotted circles are temperature markers. The diagonal straight line is the locus of solar Mo/Zr ratios. The open diamonds on this line indicate (starting from lower left), solar, 30 times solar, and 100 times solar (Mo, Zr)/Ti ratios when all three elements are completely condensed. The open diamonds on the dotted curves indicate the final grain compositions for cases of Zr removal.

starts forming. Further cooling eventually removes all Zr, Mo, and Ti from the gas, and the condensation track moves onto the solar Mo/Zr line (*open diamond*). As Figure 11 illustrates, formation of a Zr-Mo-Ti carbide alloy from a gas of *solar* composition cannot yield the Mo/Ti and Zr/Ti ratios in the carbides, since the condensation track falls well below the observed ratios.

However, if we take into account the possibility of *s*-process enrichment, the comparison becomes more favorable. Figure 11 also displays condensation curves that result when Mo and Zr abundances are uniformly elevated to simulate *s*-process additions to these elements. The initial condensation temperature of ZrC is 1890 and 1926 K for a gas with 30 and 100 times the solar Zr abundance, respectively. At 1800 and 1720 K, the Zr/Ti ratios are approximately constant in both cases and not very sensitive to the absolute Zr abundance. However, the increased Mo abundance increases the activity of MoC at any given temperature, so that more Mo dissolves in the ZrC, and the Mo/Ti and Mo/Zr ratios are correspondingly greater.

Because we have assumed that Mo and Zr are uniformly enriched, the composition will move onto the solar Mo/Zr line (Fig. 11) when all of the Zr, Mo, and Ti have condensed. It is important to note that any grains condensing from a gas with a solar Mo/Zr will have Mo/Zr ratios that are equal to or less than the solar ratio, i.e., compositions lying on or to the right of the solar Mo/Zr line in Figure 11. However, the majority of observed grains have Mo/Zr ratios that are *greater than* or equal to the solar ratio. On theoretical grounds it is not expected that the *s*-process will increase the abundance of Mo more strongly than that of Zr. The only other way to shift the condensation path to the left of the solar Mo/Zr line is by condensation of these grains in a gas from which Zr has been depleted by prior condensation and removal of Zr-rich grains.

Pursuing this possibility, in Figure 11 we give examples of what happens with early ZrC removal for the case of 100-fold enrichment in Mo and Zr, accompanied by removal of 50%, 90%, or 99% of the Zr as ZrC before the remainder of the grains form. To take a specific case: assume that ZrC begins to condense from an undepleted gas and that 50% of the total Zr condenses as ZrC. This ZrC will contain only trace amounts of Mo and Ti (0.15% and 0.003% of total Mo and Ti, respectively), so we may neglect initial depletions in these elements. Now suppose that the initially formed ZrC grains are removed from equilibrium with the gas, and that the Zr-depleted gas continues to cool and new ZrC grains form. If these grains continue to equilibrate with the gas down to temperatures where all of the remaining Zr, Mo, and Ti is condensed, the Mo/Zr ratios in these grains will be greater than solar, and the resultant compositions will lie to the left of the solar Mo/Zr line in Figure 11.

By this hypothesis, the production of carbides in which Mo is enriched relative to Zr is the result of the failure of the Zr-rich crystals that formed first to maintain equilibrium with the cooling gas. We must correspondingly suppose that a mechanism exists that causes the first crystals that form to be physically removed from contact with their parent gas. In stellar atmospheres, this process might plausibly occur if these crystals develop a positive drift velocity relative to the expanding parent gas because of radiation pressure from the star. We must also suppose that as the parent gas (now largely depleted of these crystals) moves farther from the star and cools, newly forming grains and gas are more strongly coupled to each other and subsequently evolve in equilibrium. The Zr-rich crystals that formed first are, of course, not "lost" in any absolute sense but merely transported into a cooler environment. Presumably, they may be occluded by carbon during subsequent graphite formation in this environment. Such crystals would have Mo/Zr ratios less than the solar value, consistent with the observation of Zr-rich crystals with compositions lying to the right of the solar line in Figure 11.

We note that *s*-process enrichments of Mo and Zr of 30 times solar or more are required to account for the compositions of the majority of the grains in which Zr, Mo, and Ti were detected. Comparison of the model calculations with the observations show that in some cases little or no Zr depletion is necessary (i.e., when the measured Mo/Zr ratio is nearly solar), while in other cases the depletions must range up to $\sim$90%. However, some grains (not shown in Fig. 11) are basically pure TiC. Such grains may have formed after Zr-Mo–rich grains had condensed and were removed from further equilibration, in the manner described above for Zr-rich grains. It is also possible that these grains originated from gases not strongly enriched in *s*-process elements, so that formation of refractory carbides of Zr and Mo was kinetically inhibited owing to the low abundance of these elements (cf. § 7.1). If they were nonetheless present in solid solution with TiC, they would not have been detected in our EDS analyses because of their low abundance (solar Zr/Ti = 0.005 and Mo/Ti = 0.001; Anders & Grevesse 1989).

6.3. *Condensation of Less Refractory Elements*

We also explored the extent to which the other elements detected in the internal grains (Fe, Cr, Ni, Ru; cf. Table 1) could condense into ZrC-TiC-MoC alloys. Above the graphite condensation temperature, none of these elements or their carbides dissolve in the refractory carbide alloy in any significant amounts. In fact, temperatures much lower than the graphite or SiC condensation temperatures are necessary to dissolve these elements in Zr-Ti carbide. But it is difficult to imagine that condensation of graphite was delayed to such low temperatures, given that the TEM observations tend to rule out this possibility (§ 5). In addition, the large spread of Fe, Ni, Cr, and Ru abundances and the rather random occurrence and distribution of these elements among the internal grains suggest that a process other than direct condensation is responsible for their occurrence.

We know that the graphite sometimes contains measurable concentrations of elements other than carbon. For example, we detected minor Si in EDS analysis of the graphite in most (but not all) of the spherules, although internal crystals of SiC were observed in only one instance (§ 5). Similarly, Ni was detected in the graphite from B1a, the spherule having the highest Ni/Ti ratio in its internal crystals; and Cr was detected in graphite from B1f, a spherule containing a crystal with a high Cr/Ti ratio (Table 1). It seems likely that in many cases these elements may have become dissolved or otherwise trapped in condensed carbon, and were occasionally scavenged from this material by the carbide grains.

7. KINETICS OF GRAIN GROWTH

Here we consider constraints imposed by growth kinetics on the physicochemical conditions in the environments

where the circumstellar graphites were formed. We shall not be concerned with general questions of nucleation and grain growth in stellar environments, but shall develop a formalism only to the extent required to address the specific observations that are reported here. A general treatment of nucleation and grain growth in stellar atmospheres is given by Salpeter (1974a, 1974b, 1977). Kinetic models that include reference to laboratory observations of circumstellar graphite in meteorites have been presented by Cadwell et al. (1994) and Sharp & Wasserburg (1995).

7.1. *Grain Growth Model for* TiC *and Graphite*

Following Sharp & Wasserburg (1995), we take the grain growth rate to be proportional to the mean speed and number density of gas atoms contributing to the growth. Expressing this rate partly in terms of macroscopic quantities, for growth of a monatomic solid (e.g., graphite) we have

$$\frac{dr}{dt} = \frac{\mu}{4\rho N_{\rm A}} v\bar{v} , \tag{2}$$

with the mean speed $\bar{v}$ of gaseous species given by

$$\bar{v} = \left(\frac{8kT}{\pi m}\right)^{1/2} . \tag{3}$$

Here r is the grain radius, μ and ρ are the molecular weight and density of the solid, T is the absolute temperature, $N_{\rm A}$ is Avogadro's number, k is Boltzmann's constant, and m and v are the molecular mass and number density of the gas-phase species being deposited. Because we are interested primarily in establishing upper limits to grain sizes and growth rates, we take the sticking probability of a gas molecule onto a grain upon impact to be unity, and we ignore evaporation. Grain growth rates in this model (eq. [2]) will thus be strictly maximal under the assumed conditions, since they are limited only by the rate of arrival of gas atoms at solid surfaces. The expression equivalent to equation (2) for the growth rate of a diatomic substance (e.g., TiC) from gas-phase species 1 and 2 is

$$\frac{dr}{dt} = \frac{\mu}{4\rho N_{\rm A}} \frac{v_1\bar{v}_1 v_2\bar{v}_2}{v_1\bar{v}_1 + v_2\bar{v}_2} . \tag{4}$$

Inspection of equation (4) shows that if one of the gas species is much more abundant than the other (as in the case of TiC formed from a gas with condensable C $\approx$ 1000 $\times$ Ti for C/O = 1.1), the growth rate is dictated by the availability of the less abundant species, and equation (4) reduces to equation (2).

In modeling grain growth we explicitly take into account several factors that are likely to be of importance in stellar environments. The first of these is expansion of the volume of gas in which grains are forming, as mass flows away from the star. For simplicity, we assume that this expansion is uniform and adiabatic, resulting in gas cooling [$T = T(t)$] as well as time dependence in the number density v of condensable species. The adiabatic expansion law is given by $T_0 t_0^{\alpha} = Tt^{\alpha}$, where α is related to the adiabatic index γ by $\alpha = 3(\gamma - 1)$ and t_0 is the effective time constant for expansion of the system at arbitrary reference temperature T_0. It is often convenient to use the temperature T rather than the time t as an independent variable, and we often have recourse to this later in this paper.

In our calculations we explore values of t_0 ranging from 5×10^5 s up to 5×10^8 s. For convenience we choose $T_0 = 2000$ K, above the condensation temperatures of any species we shall consider (i.e., $T < T_0$ and $t > t_0$ for all T, t), yet sufficiently close to them that we can assume an approximately constant γ of the gas in the temperature ranges of interest. At and below this T_0, for example, most hydrogen is in the form of H_2 (cf. Palla, Salpeter, & Stahler 1983). We thus take $\gamma \approx 4/3$ for gas of solar composition at T_0, so that $\alpha = 1$ and the temperature of the gas decreases in inverse proportion to expansion time. This cooling rate is somewhat more rapid than rates derived from astronomical observation (with α generally between $\frac{1}{2}$ and 1; cf. Cadwell et al. 1994; Cherchneff et al. 1992), where slower rates may be the result of radiative heating of grains in the stellar atmospheres, a complication that we shall not consider here. However, our choice of α will not strongly affect the results for the time it takes to grow a grain of a given size, but it will affect our estimate of the temperature drop in the gas during that interval.

Second, we take into account the depletion of gas species by condensate formation in the range of temperature and pressure being considered. Thus v not only depends upon the degree of expansion of the system but is also a function of the average size of grains produced within a given time [$v = v(r, t)$]. Finally, because we do not assume an infinite supply of condensable gas (in which case the grain size varies directly with growth time; eq. [2]), the ultimate size to which grains can grow depends on the number of grains per unit volume, n_g, and because of expansion this is also a function of time [$n_g = n_g(t)$]. For the most part, we will not confront the difficult problem of nucleation. We will simply assume that all nuclei for a given solid phase appear at the same temperature, and that all growing particles of a given species have the same size at any given time; however, we will also briefly note the consequences of a temporal spread in the formation of nuclei (§ 7.2).

Taking gas expansion and depletion into account, the rates of change of grain radius and number density of condensable gas are

$$\frac{dr}{dt} = cvT_0^{1/2} t_0^{\alpha/2} t^{-\alpha/2} \tag{5}$$

and

$$\frac{dv}{dt} = \frac{-\alpha}{\gamma - 1} vt^{-1} - \eta v r^2 t^{-\alpha/2 - \alpha/(\gamma - 1)} , \tag{6}$$

with the constants c and η given by

$$c = \frac{\mu}{4\rho N_{\rm A}} \left(\frac{8k}{\pi m}\right)^{1/2} \tag{7}$$

and

$$\eta = \pi \left(\frac{8k}{\pi m}\right)^{1/2} T_0^{1/2} n_{g0} t_0^{\alpha/2 + \alpha/(\gamma - 1)} . \tag{8}$$

In equation (6), the first term represents the rate of change in number density due to expansion, and the second term represents the rate of depletion of molecules in the gas phase caused by grain growth. The constant n_{g0} in equation (8) is the number of grains per unit volume at the condensation temperature, extrapolated back to the reference time t_0 (taking into account the system expansion that has

occurred). Equation (5) [the equivalent of eq. 2 for $v = v(t)$] and equation (6) are the grain growth equations coupled through the variables r and v. We solve them numerically by Runge-Kutta methods, after specifying the seed radius and the number density of the relevant gas species at the initial condensation temperature.

We shall focus on both TiC and graphite, because differences in their condensation temperatures and growth rates place more stringent constraints on the nature of their source environment than either does separately. In all calculations we assume solar elemental abundances except for C. We take C/O = 1.1 for the gas phase prior to condensation, since this is in accord with observations on carbon stars (Lambert et al. 1986; Olofsson et al. 1993) and because it is within the range of C/O that in equilibrium condensation permits TiC to condense before or during graphite condensation (§ 6.1), consistent with the TEM observations (§ 5). We consider only the condensable carbon in the gas phase, that is, C not tied up in CO during graphite and TiC formation (mostly present as C_2H_2; Table 2). We also use equilibrium model results (§ 6.1; Sharp & Wasserburg 1995: Lodders & Fegley 1995) as a guide to condensation temperatures in the grain growth calculations (Table 2). Because of nucleation effects, minerals may begin condensing at somewhat lower temperatures than those given by equilibrium calculations, but under conditions of gradual monotonic cooling the sequence in which minerals form and the temperature interval separating their appearance are unlikely to be strongly affected (e.g., Lodders & Fegley 1992). Moreover, the TEM observations (§ 5) unambiguously show that TiC and graphite typically condensed prior to SiC, a result fully consistent with the condensation sequence established by equilibrium thermodynamics under astrophysically plausible pressures and C/O ratios (Table 2).

In Figure 12 we plot examples of r, v, and T as a function of time to illustrate the main features of the solutions to equations (5) and (6). If n_g is sufficiently large, gas depletion accompanies grain growth as the seeds accrete the available gas, v decreases rapidly, and the grain size soon reaches a maximum (r_{max}) as the gas cools below the initial condensation temperature. The maximum size of the grains, r_{max}, increases as n_g decreases, and in the limit that few grains are present (n_g and $\eta \rightarrow 0$), v is reduced only by adiabatic expansion and falls off slowly, leading to larger grains for any specific temperature drop. We also compare the results for equation (2), where v is held constant and the grain size increases nearly linearly in time (the small departure from linearity is due to the weak $T^{1/2}$ dependence).

According to equation (6), the rate of gas-phase depletion depends on the number density of developing grains (n_g) as well as on the gas-phase number density v of elements of interest (C and Ti). To estimate upper bounds on n_g, we assume that all grains of a given mineral grow to the same size, and that grain growth is ultimately limited only by gas-phase abundances. Thus n_g(max) for graphite is found by comparing the number of atoms of C in grains of a representative size to the number density of condensable C in the gas phase at a given total pressure P (Table 2). The circumstellar graphite size distribution is sharply peaked near 1 μm, and, since a spherule of this size contains about 6×10^{10} atoms of C, n_g(max) for graphite is ~ 1 cm^{-3} at the

TABLE 2

GRAIN GROWTH MODEL INPUT PARAMETERS

A.

Parameter	Assumed Value
C/O (atomic)	1.1
(Condensable C)/Ti (atomic)	992
$\mu_{graphite}$ (g mole^{-1})	12
μ_{TiC} (g mole^{-1})	59.9
$\rho_{graphite}$ (g cm^{-3})	2.25
ρ_{TiC} (g cm^{-3})	4.91
Graphite seed radius (cm)	5×10^{-7}
TiC seed radius ($\sim$200 molecules) (cm)	1×10^{-7}
Condensable species	C_2H_2, Ti
Reference temperature T_0 (K)	2000
Timescale for system expansion t_0 (s)	5×10^5–5×10^8
Molecular weight of gas phase at $T \leq T_0$ (g mole^{-1})	2.34

B.

Total Pressure (dynes cm^{-2})	Equilibrium Condensation Temperature[a] (K)			Number Density[b] at T_{gr} (cm^{-3})		Maximum Number of Graphite Grains[d] (cm^{-3})
	Graphite	TiC	SiC	Condensable C[c]	Ti	
0.001	1620	1430	1260	6.4×10^5	6.5×10^2	10^{-5}
0.01	1640	1490	1325	6.3×10^6	6.4×10^3	10^{-4}
0.1	1660	1560	1390	6.2×10^7	6.3×10^4	10^{-3}
1.0	1670	1640	1465	6.2×10^8	6.2×10^5	10^{-2}
10	1680	1715	1545	6.2×10^9	6.2×10^6	10^{-1}
100	1680	1790	1630	6.2×10^{10}	6.2×10^7	1

[a] Approximate temperature of initial condensation from Lodders & Fegley 1995.

[b] Number density of gas phase species at C/O = 1.1; T_{gr} = condensation temperature of graphite at stated pressure.

[c] Carbon in excess of that tied up in CO.

[d] Approximate maximum number density of 1 μm graphite grains for C/O = 1.1. The corresponding maximum values for 10 nm TiC grains are roughly 2×10^3 times greater at any given pressure.

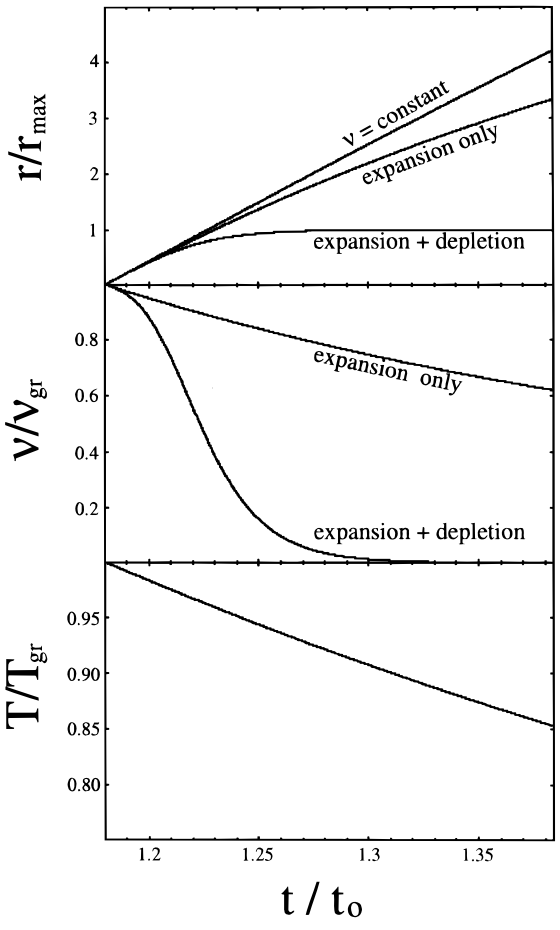

FIG. 12.—Sample solutions to eqs. (5) and (6) illustrating the variation of graphite spherule radius (r), condensable gas number density (v), and temperature (T) as a function of time (t), for system expansion alone and for expansion accompanied by C depletion due to grain growth. Also shown is the variation of grain radius with time when v is held constant but system temperature decreases (eq. [2]). The radius of the grain, r, is in units of the maximum radius (r_{max}) attainable when both expansion and depletion are taken into account; v_{gr} and T_{gr} are the number density of condensable C and the temperature at the start of graphite condensation, respectively; t_0 is the system expansion timescale at reference temperature $T_0 = 2000$ K. Assumed parameters were $t_0 = 10^7$ s and $P = 1$ dyne cm^{-2} (cf. Table 2), with $n_g = 3 \times 10^{-3}$ cm^{-3}.

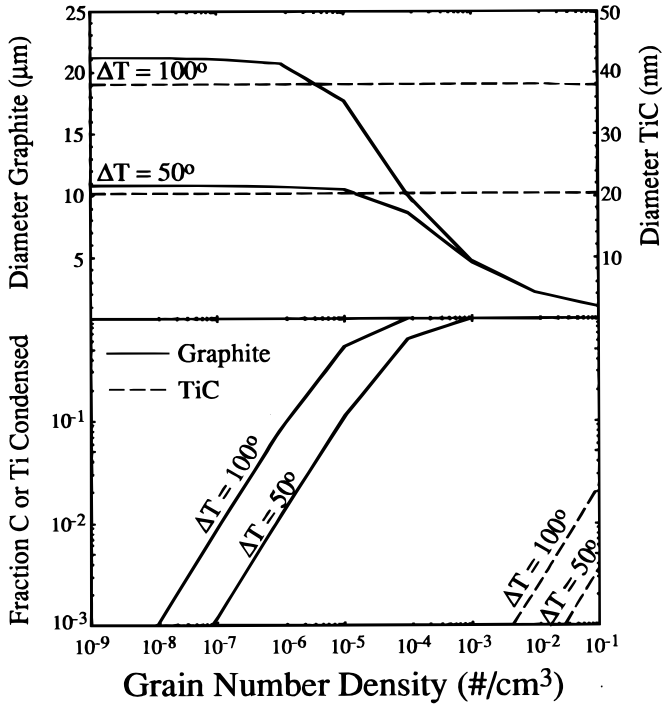

FIG. 13.—Variation of TiC (*dashed lines*) and graphite (*solid lines*) grain size and fraction of available C and Ti condensed, as a function of the number density of grains and temperature drop ΔT measured from the start of condensation. Assumed parameters were $t_0 = 10^7$ s and $P = 10$ dynes cm^{-2} (cf. Table 2).

highest total pressure we consider ($P = 10^2$ dynes cm^{-2}) and $\sim 10^{-5}$ cm^{-3} at the lowest ($P = 10^{-3}$ dynes cm^{-2}). For TiC, with a modal size of ~ 10 nm (2.6×10^4 atoms Ti), n_g(max) is roughly 2×10^3 times larger at any P.

Inspection of equations (5) and (6) shows that although the rate of gas-phase depletion varies directly as n_g, it also depends strongly on the number density of condensable gas molecules controlling the growth. Since condensable carbon is roughly 1000 times more abundant than Ti (for C/O = 1.1; Table 2), the rate of TiC growth is limited by the gas number density of Ti (cf. eq. [4]), and the formation of graphite will not control the growth rate of TiC unless essentially all of the carbon is scavenged from the gas. Not only will the growth rate (dr/dt) of graphite be far larger than that of TiC (by a factor of $\sim 10^3$), but the rate of gas-phase depletion of carbon during graphite growth will be correspondingly much more rapid than the rate of Ti depletion during TiC growth, for any given value of n_g.

Figure 13 illustrates the effect of n_g on graphite and TiC grain sizes and on the fraction of C and Ti condensed within a given temperature drop ΔT below their initial condensation temperatures (at $P = 10$ dynes cm^{-2}). For larger values of n_g, graphite reaches a maximum size within a small ΔT and, because of the high number density of grains, scavenges all of the condensable carbon. For n_g below a limiting value, on the other hand, the graphite size varies in proportion to ΔT because the fraction of C condensed is negligible. The limiting value of n_g for TiC is clearly much greater, and indeed we find that depletion of Ti due to the formation of 10 nm sized grains is not important until n_g exceeds the maximum value for graphite (Table 2) by a factor of 10^3. For the entire range of n_g depicted in Figure 13, there is almost no Ti depletion, and the TiC grain size is proportional to ΔT. In cases of low n_g, however, the condensation of SiC imposes restrictions on the range of ΔT and thus on the sizes to which graphite and TiC grains can grow. As discussed previously (§ 5), SiC will usually form at the expense of previously condensed graphite. At the temperature at which SiC begins to form, there should be little Ti remaining in the gas phase, unless there are kinetics limitations. Regardless, the remaining Ti will preferentially go into solid solution with SiC (Lodders & Fegley 1995), effectively quenching the growth of any preexisting TiC grains. Inspection of Table 2 shows that the temperature interval ΔT between initial graphite and SiC condensation varies from $\Delta T \approx 360$ K at $P = 10^{-3}$ dynes cm^{-2} down to $\Delta T \approx 50$ K at $P = 10^2$ dynes cm^{-2}; in contrast, for pressures within this range TiC always condenses at 160–170 K above the SiC condensation temperature (cf. Fig. 10; Fegley 1982; Sharp & Wasserburg 1995; Lodders & Fegley 1995).

In Figure 14 we display growth times (as a function of total gas pressure) required to produce 1 μm graphite spherules (line *a*) and 10 and 30 nm TiC grains (lines *c* and *d*)

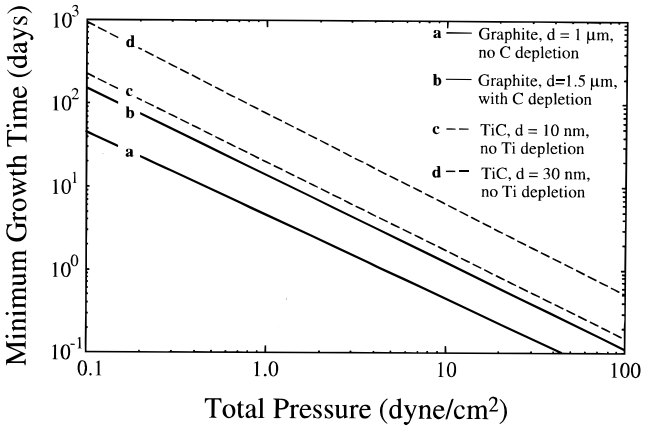

FIG. 14.—Strict minimum growth times (i.e., assuming perfect sticking efficiency of impinging gas species and no subsequent evaporation) required to achieve various final grain sizes as a function of total gas pressure, using the assumed values in Table 2. Solid lines are for graphite, dashed lines for TiC. Conditions of formation for grains of various diameters are as noted in the figure.

when condensable gas depletion is negligible. Because of this assumption, and because perfect sticking efficiency of gaseous species and no evaporation are assumed, the displayed times are strict lower bounds on the actual times that would be required to achieve these grain sizes. Only total pressures $P \geq 0.1$ dynes cm^{-2} are shown, because below this pressure ΔT for TiC exceeds the limits discussed above for any value of t_0 (the timescale for expansion of the system) within the range given in Table 2. Even at $P = 0.1$ dynes cm^{-2}, TiC growth to 10 nm is possible only at the slowest expansion timescale considered ($t_0 = 5 \times 10^8$ s).

Inspection of Figure 14 shows that TiC growth places the most stringent constraints on gas pressure in the grain growth environment. Under the most rapid growth conditions possible, it takes $\sim$0.6–2.5 yr to grow 10–30 nm TiC grains at pressures of 0.1 dynes cm^{-2}; at this same pressure, 1 μm graphite spherules may be grown in $\sim$2 months (neglecting carbon depletion). These timescales are in basic agreement with, although slightly longer than, those in previous calculations by Sharp & Wasserburg (1995), which were arrived at through equation (2) and did not include system expansion. Under realistic growth conditions (with less than unit sticking efficiency and evaporative loss of condensed material), it is clear that pressures significantly higher than 0.1 dynes cm^{-2} are required to grow $\sim$10 nm TiC grains in times on the order of a year.

In Figure 14 (line *b*) we also display the results for graphite growth when gas-phase depletion of C is included, so that the size of the graphite when all condensable C is used up corresponds to the modal diameter of $\sim$1.5 μm (Fig. 1). The n_g required to produce spherules of this size ranged from 3×10^{-4} cm^{-3} at 0.1 dynes cm^{-2} to 0.3 cm^{-3} at 100 dynes cm^{-2} at the graphite condensation temperature. These grain number densities correspond to a graphite dust-to-gas mass ratio of $\sim 7 \times 10^{-4}$. We observe that comparable timescales are required to produce graphite and TiC grains with diameters corresponding to their modal values of 1.5 μm and 10 nm (Fig. 14) when gas depletion is significant for C but not for Ti. As noted above, this will be the case as long as the number density of TiC grains is not more than about 10^3 times greater than the number density of graphite grains.

We have seen that at pressures less than about 0.1 dynes cm^{-2}, grains cannot grow to the observed sizes as the gas temperature falls through the ranges required by equilibrium thermodynamics, even assuming optimal growth. This problem may also be phrased in terms of growth times, in that *minimal* timescales of $\sim$1 yr are required at 0.1 dynes cm^{-2}, which is of the same order of magnitude as plausible grain residence lifetimes in a stellar atmosphere. The problem becomes worse at lower pressures, of course. To cite one example from low-mass AGB models, in the atmosphere of stars with nominal mass-loss rates of 10^{-6} to 10^{-5} $M_\odot$ yr^{-1}, the density is typically thought to be $\sim 10^{-14}$ g cm^{-3} ($P \sim 10^{-3}$ dynes cm^{-2}) in the region where temperatures are low enough for grain formation to ensue (Bowen 1988; Fleischer, Gauger, & Sedlmayr 1992; Cherchneff et al. 1992). At this density it would take no less than $\sim$60 yr for 10 nm TiC grains to grow. On the other hand, at a wind speed of $\sim$15 km s^{-1} characteristic of mass outflow from such stars (Zuckerman, Dyck, & Claussen 1986), grains can escape the star in roughly a tenth of this time.

Thus, given the pressure and time requirements dictated by application of either equilibrium thermodynamics or kinetics to the TEM observations, it does not seem possible to grow the refractory carbide grains under the conditions generally assumed to obtain in spherically symmetric AGB atmospheres that are losing mass at typical rates. This problem has been recognized already by Sharp & Wasserburg (1995). The problem of inadequate timescales available for growth could perhaps be evaded within long-lived disks or envelopes around binary star systems (cf. Iben 1991), such as in the environment around the Red Rectangle described by Jura, Balm, & Kahane (1995). However, postulating the role of such envelopes in the growth of graphite spherules and TiC cannot evade the problem of the pressures imposed by equilibrium thermodynamics; one must also suppose that the pressures in long-lived envelopes are high ($\gtrsim$0.3 dynes cm^{-2}; cf. § 6.1).

The growth problem would be worse than we have indicated if we had assumed less than unit sticking efficiencies for impinging gas species, since any decreases in sticking efficiency can be effectively compensated for only by corresponding increases in gas pressure. The fact that TiC (and Zr, Mo carbide) grains exist at all must therefore imply that sticking efficiencies cannot be far less than unity, despite theoretical assertions to the contrary (e.g., Johnson, Friedlander, & Katz 1993). Note that the situation is also not helped by assuming a higher C/O ratio, because, as C/O increases, so does the total pressure required to allow TiC to condense prior to graphite. If C/O increases just from 1.1 to 1.3, the minimum total pressure required for formation of TiC prior to graphite increases by an order of magnitude (cf. Fig. 10).

Although we have not considered the formation of other carbides explicitly, it is straightforward to extrapolate the results for TiC to the case of ZrC. The solar abundance of Zr is about 200 times less than that of Ti (Anders & Grevesse 1989), so the growth of ZrC grains is kinetically less favorable than the formation of TiC grains. On the other hand, if there is an enhancement in the Zr abundance due to *s*-process contributions, then ZrC grains may be able to form. For example, assuming an *s*-process enhancement of Zr relative to Ti that is 100 times solar (cf. § 6.2), for a given deposition time and total pressure ZrC grains will grow to

about half the size of TiC grains. The size disparity will naturally become greater for smaller *s*-process enrichments. It is thus not surprising that more than two-thirds of the carbides with diameters greater than 10 nm are Ti-rich (i.e., Zr/Ti < 1), while more than half of the carbides with diameters ≤ 10 nm are Zr-rich (cf. Table 1).

7.2. *Effect of Temperature on Grain-Size Distribution*

Thus far we have considered only the conditions required to produce grains of the most commonly observed sizes (modal sizes of 1.5 μm for graphite and 10 nm for TiC). However, substantially larger grains are also observed (Fig. 1 and Table 1), and it is appropriate to ask to what extent the observed distribution of graphite grain sizes reflects differences in grain formation conditions. Instead of assuming that all grains appear simultaneously and grow to a uniform size, we now explore the consequences of supposing that there is a maximum in the rate of appearance of seeds at some mean temperature $T_{\rm mean}$ below the equilibrium condensation temperature. For simplicity, we will assume that the distribution in the number of seeds dn_g/dT formed near this temperature approximates a normal distribution (cf. Draine & Salpeter 1977). The earliest graphite grains to form will therefore grow to be the largest, because initially there will be little C depletion in the gas, but grains formed later will be smaller because of gas-phase depletion of carbon as well as a smaller time interval available for growth at lower ambient pressures. Assuming that the nucleation rate depends on the square of the number density $v_{\rm C}$ of condensable carbon (cf. McDonald 1963), the final size distribution dn_g/dr will be related to the temperature (time) dependence of the grain size dr/dT by

$$\frac{dn_g}{dr} \propto v_{\rm C}^2 \frac{dn_g}{dT} \Big/ \frac{dr}{dT} . \tag{9}$$

To approximate the C depletion behavior resulting from the temporal spread in seed appearance, we solve equations (5) and (6) assuming no condensible C depletion ($\eta = 0$) when $T > T_{\rm mean}$, but allowing for depletion when $T \leq T_{\rm mean}$. We then normalize the peak in the model size distribution (eq. [9]) to the maximum in the real distribution (Fig. 1), with the variance of the dn_g/dT distribution tuned to provide the best fit to the observed graphite size distribution. Figure 15 shows an example of how the final graphite diameter depends on the relative temperature at which seed formation occurred (*dotted curve*), and how the model size distribution (eq. [9], *solid curve*) compares to the actual distribution. In this example $\sim 99\%$ of the seeds appear within about ± 10 K of $T_{\rm mean}$. Although the model can reproduce the size distribution of graphites $\lesssim 2.5$ μm ($\sim 80\%$ of the grains), it cannot account for the observed frequency of larger grains. This exercise is, of course, a phenomenological one not based on first principles, since it does not address the thermodynamics of nucleation or the occurrence of carbide heterogeneous nucleation centers that were observed in some grains (§ 5). But qualitatively it appears that the largest graphite grains in the observed size distribution imply much higher carbon number densities and/or longer deposition times than those required to produce the modal size (1.5 μm), whereas the size distribution of smaller grains about this mode could be produced with only a small spread in seed formation temperatures under fairly uniform conditions. These conclusions are consistent with the inferences derived from considerations of graphite rim thicknesses observed in ultrathin sections, as discussed in § 4.

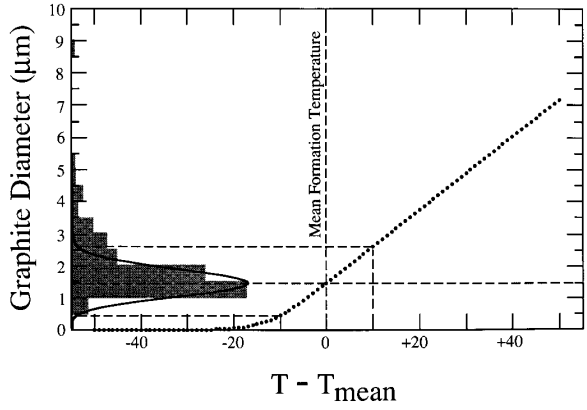

FIG. 15.—Example of the variation of graphite diameter (*dotted curve*) at the end of condensation as a function of seed appearance temperature, assuming a peak in seed formation at $T = T_{\rm mean}$. The solid curve is the model size distribution given by eq. (9), superposed on the actual size distribution of onion-type circumstellar graphites (from Fig. 1). In this example, $\sim 99\%$ of the seeds form within ± 10 K of the mean appearance temperature. Assumed parameters were $t_0 = 5 \times 10^6$ s, $n_g = 0.03$ cm^{-3}, and $P = 10$ dynes cm^{-2}, with $T_{\rm mean}$ taken to be 50 K below the equilibrium condensation temperature at this pressure (cf. Table 2).

7.3. *Grain Clusters*

We have now shown that the equilibrium condensation sequence of refractory carbides included within graphite requires "high" pressures ($\gtrsim 0.1$ dynes cm^{-2}) and that the time requirements imposed by kinetics for growing grains of the observed sizes lead to the same conclusion. A third observation consistent with this conclusion is that in some graphites not just single carbide grains, but *clusters* of carbide grains, served as heterogeneous nucleation centers for carbon condensation. An example is Figure 7*b*, showing a central cluster of four 10 nm TiC grains. We observed central clusters in three other graphite grains. For such carbide clusters to form, there must be a high enough number density of grains to permit them to come into contact before graphite condensation is complete. Considering the requirements for pairs of TiC grains with diameters $d = 10$ nm to come into contact, we note that the mean free path between such encounters is given by $\lambda = 1/(2^{1/2} n_g \sigma)$, within collision cross section $\sigma = \pi d^2$. A lower bound on the mean free path ($\lambda_{\rm min}$) is obtained using n_g(max) as described above, which gives $\lambda_{\rm min} \approx 10^{13}$ cm at $P = 10^{-3}$ dynes cm^{-2} and $\lambda_{\rm min} \approx 10^8$ cm at $P = 10^2$ dynes cm^{-2}. Taking the average speed of the 10 nm grains as ~ 300–500 cm s^{-1} corresponding to a kinetic temperature of ~ 1600 K, and a typical timescale on the order of a year for the formation of the grains, they will be able to travel a distance of $\sim 10^{10}$ cm, which is the minimum collision mean free path between grains at their maximum number density for $P \sim 1$ dyne cm^{-2}. Thus, to account for the observed clusters of carbide grains in the spherules, we may take $P \gtrsim 0.1$ dynes cm^{-2} as a conservative lower bound on the total pressure in the regions of grain formation. The gas pressures required to account for the observed carbide grain assemblages are thus consistent with the previously derived pressure constraints. Of course, if mechanisms exist for moving grains of the same size with relative speeds substan-

tially greater than thermal speeds, the inferred pressures would be lower. Biermann & Harwit (1980) investigated grain collisions in red giant atmospheres, and argue that relative grain speeds on the order of kilometers per second are possible. In the context of the above argument, this would lower the pressure requirement by several orders of magnitude (provided the grains would stick together rather than fragment at such relative speeds; cf. Salpeter 1974a). In their model these relative speeds are the result of the effect of radiation pressure on grains of *different* sizes, however, with larger grains overtaking smaller ones. Moreover, at pressures as low as those taken to characterize atmospheres of low-mass AGB stars at temperatures suitable for grains to condense ($\sim 10^{-3}$ dynes cm^{-2}; Bowen 1988; Fleischer et al. 1992), the *minimum* mean free path between collisions of TiC grains ($\sim 150\ R_\odot$) is of the same order as a stellar radius. Under such conditions the aggregation of TiC grains before carbon condensation is implausible.

7.4. *Inferred Stellar Mass-Loss Rates*

In seeking to relate the physical conditions under which carbide and graphite grains can form to the astrophysical environments in which the grains that we have in hand actually did form, we are led to consider stellar mass-loss rates. Our purpose is not to construct a detailed stellar atmosphere model with mass loss, but simply to estimate the mass-loss rates implied by our observations and compare them to the rates inferred for real stars. We assume that the mass-loss rate ($\dot{M}$) through a shell in the stellar atmosphere at radius R is related to the density $\rho(R)$ by

$$\dot{M} = 4\pi\rho(R)R^2 v\ , \tag{10}$$

where v is the speed of radial expansion at R, and $\dot{M}$ is usually given in $M_\odot$ yr^{-1}. Mass-loss rates for stars are given by parameterizations of astronomical observations, usually in terms of the stellar radius, mass, and luminosity (summarized by Chiosi & Maeder 1986). The mass-loss rates for red giants and supergiants range from a lower observational limit of $10^{-8}\ M_\odot$ yr^{-1} up to as much as $10^{-4}\ M_\odot$ yr^{-1} (e.g., Iben & Renzini 1983; Blöcker 1995).

We simply use the sound speed (~ 3.4 km s^{-1}) at reference temperature T_0 (2000 K) as an estimate of the mass outflow speed v at the time that grains start to form, even though radiation pressure may later accelerate grains to their terminal outflow speeds of 10–20 km s^{-1}. For any assumed value of $\rho(R)$ [or $P(R)$] and R, we may then solve equation (10) for $\dot{M}$, with the results shown in Figure 16. We also plot t_0, the expansion timescale at T_0, assuming $t_0 \approx R/v(T_0)$. With appropriate values for the density (pressure) at the time of grain formation and $\dot{M}$, equation (10) yields values of R compatible with those from Bowen's (1988) models for low-mass AGB star atmospheres. Also highlighted in Figure 16 are the parameter fields in which graphite and TiC can grow to their characteristic sizes, under the same conditions discussed above in relation to Figure 14. For $\dot{M} \approx 10^{-5}\ M_\odot$ yr^{-1}, the least restrictive growth condition (graphite with $d \approx 1$ μm, no C depletion) requires $P \gtrsim 0.5$ dynes cm^{-2}, while the most restrictive

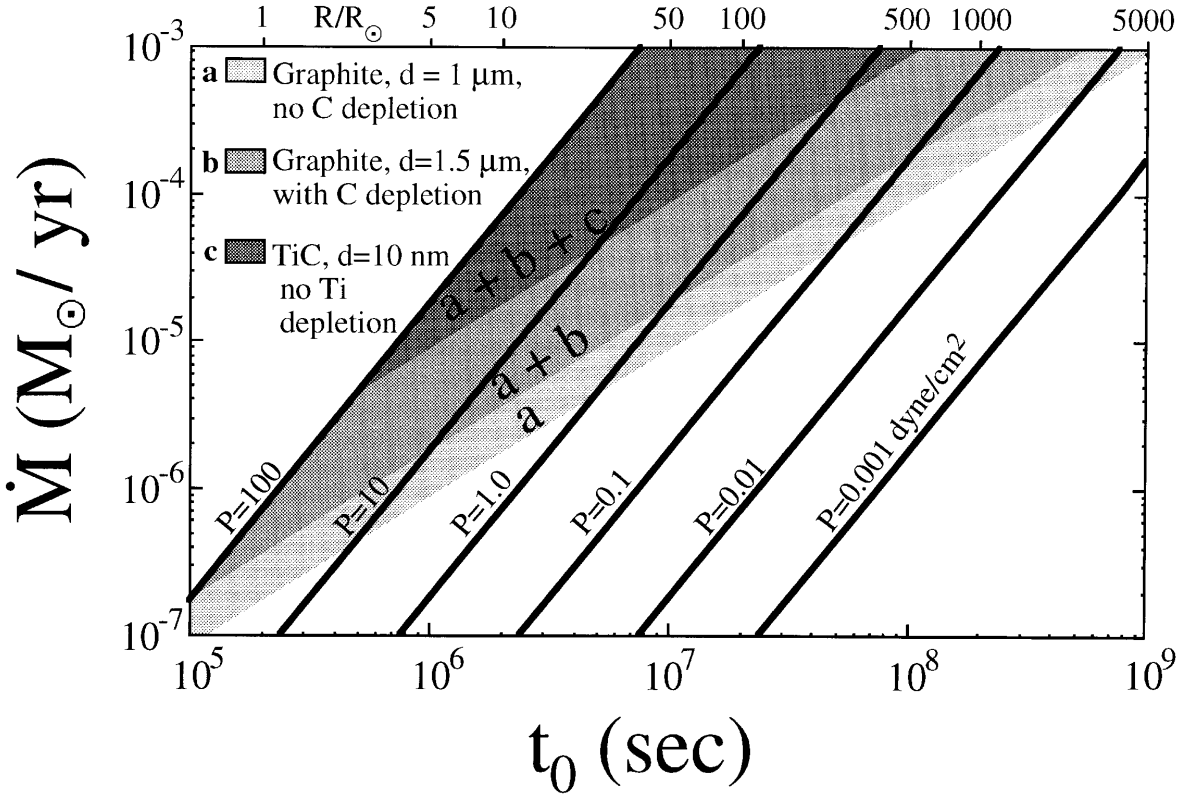

FIG. 16.—Mass-loss rates as a function of system radius (upper abcissa scale) and total gas pressure (10^{-3} dynes cm^{-2} $\leq P \leq 10^2$ dynes cm^{-2}), calculated using eq. (10). Also shown is the characteristic system expansion timescale t_0 at reference temperature $T_0 = 2000$ K (*lower abscissa scale*). Superposed on the graph are the allowed parameter fields (*shaded areas*) within the stated pressure range for the production of (*a*) 1 μm graphite grains, assuming no depletion of condensable C; (*b*) graphite grains with the KFC1 modal size of 1.5 μm, assuming condensable C depletion did occur; (*c*) 10 nm TiC grains, assuming no Ti depletion.

(growth of 10 nm TiC) requires pressures 2 orders of magnitude larger. Inspection of Figure 16 shows that under typical conditions that satisfy the $\dot{M}$ ($\lesssim 10^{-5}\ M_\odot\ \mathrm{yr}^{-1}$) and P ($\lesssim 10^{-3}$ dynes cm^{-2}) taken to characterize the atmospheres of low-mass AGB stars, neither TiC nor graphite can grow to the required sizes.

These results are consistent with the findings of Fleischer et al. (1992), who used a consistently coupled hydrodynamic and grain growth code to model the formation of carbon grains in circumstellar atmospheres of long-period variable carbon stars; for $\dot{M} \sim 10^{-5}\ M_\odot\ \mathrm{yr}^{-1}$, their model produced mean grain diameters of only ~ 0.1 μm. Note that we sometimes find even *titanium carbide* grains of this size in the graphites (Table 1). Because the cosmic abundance of C is far greater than that of Ti (by more than 10^3), this underlines the challenge to models of grain growth in trying to account for the existence of such large circumstellar grains. TiC growth always imposes the highest mass-loss rates for any given pressure, and Figure 16 shows that pressures $\gtrsim 5$ dynes cm^{-2} are required to produce TiC grains if, in accord with astronomical constraints, mass-loss rates are restricted to $\dot{M} \lesssim 10^{-4}\ M_\odot\ \mathrm{yr}^{-1}$.

In § 2.1 we noted that 25% of the graphites have $^{12}C/^{13}C$ ratios less than 89, the solar value. Assuming that these graphites formed around AGB stars, as their carbon isotopic ratios and the composition of *s*-process Kr imply, then (as we have argued above) relatively high densities must prevail in the stellar atmospheres. It is important to note that if the radius R at which condensation takes place is to have a dimension typical of red giant stars (at least several hundred $R_\odot$), the TiC growth constraint requires mass-loss rates significantly higher than $10^{-4}\ M_\odot\ \mathrm{yr}^{-1}$ (Fig. 16). Such rates are far greater than those associated with the normal winds from red giants (e.g., Blöcker 1995); if we therefore suppose that some graphite and carbide grains are produced in the atmospheres of stars losing mass through the normal winds that prevail during most of the AGB phase, we must simply abandon the attempt to apply the grain growth constraints to a spherically symmetric steady state atmosphere in its entirety. The only escape from this conclusion is to assume that outflow speeds in the grain formation region are subsonic by several orders of magnitude. But if the outflow speed there is similar to the sound speed (cf. Cherchneff et al. 1992), we must suppose instead that the grain growth pressures and timescales are those associated with *density concentrations* within such stellar atmospheres, e.g., clumps of material sporadically ejected from the star.

Clumps could have the characteristics required by the grain growth and astronomical constraints, namely, high density accompanied by short expansion timescale, initially small length scale, and reduced mass-loss rate. For example, clumps with $P \gtrsim 10$ dynes cm^{-2} and effective mass-loss rates $\lesssim 3 \times 10^{-5}\ M_\odot\ \mathrm{yr}^{-1}$ that are capable of producing 10 nm TiC grains would have characteristic expansion timescales $\lesssim 2$ months and length scales much less than a stellar radius ($\lesssim 20\ R_\odot$; Fig. 16). Spectral evidence for silicate grains around oxygen-rich stars with $\dot{M} \lesssim 10^{-5}\ M_\odot\ \mathrm{yr}^{-1}$, coupled with the apparent impossibility of nucleating and growing grains under the inferred atmospheric densities, also led Salpeter (1977) and Draine (1979) to postulate the existence of density clumps in stellar outflows. Although the existence of such density concentrations is conjectural, we note that there is substantial astronomical evidence for episodic mass loss from AGB stars (e.g., Zijlstra et al. 1992; Young, Phillips, & Knapp 1993) as well as observational evidence for density clumps in circumstellar envelopes (cf. Huggins 1994).

Alternatively, we might suppose that some graphite and carbide grains are grown during the brief "planetary nebula" phase at the end of AGB evolution, when the stellar luminosity reaches a critical value and a dramatic increase in mass-loss rate (a "superwind" phase) occurs. In superwinds, average mass-loss rates may possibly approach $10^{-3}\ M_\odot\ \mathrm{yr}^{-1}$ (cf. Iben & Renzini 1983), implying correspondingly higher atmospheric densities. Even at this high mass-loss rate, growth of 10 nm TiC grains is still restricted to gas parcels at high pressures ($\gtrsim 0.5$ dynes cm^{-2}) with length scales less than or marginally equal to a stellar radius (Fig. 16). Here again, it appears necessary to postulate the existence of density concentrations in the outflowing matter.

Silicon carbide is another species of circumstellar grain in the Murchison meteorite that is more abundant (~ 6 ppm) than graphite ($\lesssim 1$ ppm). Nearly all of this SiC ($\sim 95\%$ by mass) is in the same size range as the circumstellar graphite (0.3–3 μm; Amari et al. 1994), and isotopic studies of both major and minor elements have convincingly shown that most of it ($\sim 99\%$) was produced in AGB stars (Anders & Zinner 1993). It is therefore important to our discussion of mass loss from AGB atmospheres to consider the conditions required to form micron-sized SiC. It is sufficient to observe that for any C/O > 1.04, condensable C is more abundant than Si. Aside from any condensation details, SiC cannot grow any faster than is dictated by the rate of arrival of gaseous Si to grain surfaces (cf. eq. [2]); thus the maximum growth rate of SiC cannot be greater than the maximum growth rate of graphite. This means that SiC growth imposes pressure constraints on grain formation in AGB atmospheres somewhat more stringent than those derived from considerations of graphite growth (although less stringent than those from TiC growth). Virag et al. (1992) were similarly forced to conclude, from growth rate and size considerations, that much of the circumstellar SiC found in meteorites must have formed in sporadic, dense jets in AGB atmospheres or during the "planetary nebula" stage of these stars.

The above discussion has been restricted to outflows from AGB stars, but the requirements of high gas pressure imposed by kinetics and equilibrium thermodynamics extend to supernova ejecta as well. The conditions in such outflows should be favorable to growth of grains (as predicted by Clayton 1978), because clumping and mixing of matter due to Rayleigh-Taylor instabilities are expected to arise as a natural consequence of the mass ejection (Fryxell, Müller, & Arnett 1991; Herant & Benz 1992; Herant & Woosley 1994). There is indeed observational evidence for mixing and clumping in SN 1987A (Haas et al. 1990). Growth of graphite supernova condensates in ejecta from SN 1987A has been modeled by Kozasa, Hasegawa, & Nomoto (1989), although they were able to grow grains only up to ~ 0.1 μm in diameter. Nonetheless, the presence of ^{28}Si excesses in some graphites (cf. § 2.2) convincingly shows that they formed in supernova ejecta, after remnants of the C-rich outer zones had mixed with material from inner zones. The existence of such graphites broadly implies that as C-rich ejecta parcels reached temperatures permissive of grain growth, they must still have had sufficiently high carbon number densities ($\gtrsim 10^8$ cm^{-3}) and matter den-

sities (say $\rho \gtrsim 10^{-12}$ g cm^{-3}) to result in the formation of micron sized graphite in timescales of no more than a few years.

8. CONCLUSION AND FUTURE PROSPECTS

We have shown that microanalysis of circumstellar graphite from meteorites yields detailed information on the composition, size distribution, microstructure, and other properties of grains (and grains within grains) formed in carbon-rich circumstellar environments. Many of the observed minerals are sufficiently scarce that the prospect for observing them astronomically is slight. Thus, the observations reported here are useful in constraining the types of minerals that may be conceived to form. Many authors have speculated, for example, that SiC grains will serve as condensation nuclei for graphite and other carbonaceous grains in stellar outflows, but the data do not support this idea. Interpreted with the help of equilibrium thermodynamics and kinetic theory, the observations of circumstellar grains from meteorites provide information about the relative formation sequence of various mineral species, and lead to quantitative inferences about the chemical and physical conditions in the stellar grain formation environments.

There were, however, important limitations imposed by our experimental plan. It must not be forgotten that our study was conducted in order to survey the properties of a large number of graphite grains, without the benefit of corresponding isotopic data for each of the grains studied in the TEM. The carbon isotopic ratios in the graphites, obtained from another aliquot of this material, range over many orders of magnitude. This implies that the data reported here represent an averaging over grains from probably many different stars. The isotopic data obtained for Ne, Kr, Ti, Ca, and Si further indicate that several different types of stellar sources, including supernovae, likely contributed to the graphite suite. It is now desirable to explore how the chemical compositions and other properties of the grains depend on the particular type of stellar environment in which they formed (e.g., in supernova ejecta versus AGB atmospheres). Thus, further progress will require both mineralogic and isotopic characterization of the *same* individual grains.

We have benefited from discussions with C. Alexander, P. Fraundorf, R. Gallino, K. Kelton, G. Kurat, S. Messenger, F. Podosek, R. Walker, G. Wasserburg, and E. Zinner. T. B. would also like to thank J. Foote for invaluable assistance in the preparation of grain mounts, and to acknowledge the pioneering efforts and vision of Edward Anders and Robert Walker in the extraction and microanalysis of circumstellar grains from meteorites. This work was supported by the following grants: NSF EAR-9316328 (T. B.), NASA NAGW-3371 (T. B., S. A.), NASA NAGW-2304 (T. B.), NASA NAGW-2861 (K. L., B. F.), and NASA NAGW-3342 (R. L.).

REFERENCES

Allamandola, L., Tielens, A., & Barker, J. 1989, ApJS, 71, 733
Amari, S., Anders, E., Virag, A., & Zinner, E. 1990, Nature, 345, 238
Amari, S., Hoppe, P., Zinner, E., & Lewis, R. 1993, Nature, 365, 806
———. 1995a, Meteoritics, 30, 679
Amari, S., Lewis, R., & Anders, E. 1994, Geochim. Cosmochim. Acta, 58, 459
———. 1995b, Geochim. Cosmochim. Acta, 59, 1411
Amari, S., Zinner, E., & Lewis, R. 1995c, in Nuclei in the Cosmos III, ed. M. Busso, R. Gallino, & C. Raiteri (New York: AIP)
Amari, S., Zinner, E., Lewis, R., & Woosley, S. 1995d, Lunar Planet. Sci., 26, 37
Anders, E., & Grevesse, N. 1989, Geochim. Cosmochim. Acta, 53, 197
Anders, E., & Zinner, E. 1993, Meteoritics, 28, 490
Bernatowicz, T., Amari, S., Zinner, E., & Lewis, R. 1991, ApJ, 373, L73
Bernatowicz, T., Fraundorf, G., Tang, M., Anders, E., Wopenka, B., Zinner, E., & Fraundorf, P. 1987, Nature, 330, 728
Bernatowicz, T., Gibbons, P., & Lewis, R. 1990, ApJ, 359, 246
Biermann, P., & Harwit, M. 1980, ApJ, 241, L105
Blanco, A., Fonti, S., & Orofino, V. 1995, ApJ, 448, 339
Blöcker, T. 1995, A&A, 297, 727
Boersch, H., Geiger, J., Imbusch, A., & Niedrig, N. 1966, Phys. Lett., 22, 146
Bowen, G. 1988, ApJ, 329, 299
Cadwell, B., Wang, H., Feigelson, E., & Frenklach, M. 1994, ApJ, 429, 285
Cherchneff, I., Barker, J., & Tielens, A. 1992, ApJ, 401, 269
Chiosi, C., & Maeder, A. 1986, ARA&A, 24, 329
Clayton, D. 1978, Moon Planets, 19, 109
Czyzak, S., Hirth, J., & Tabak, R. 1982, Vistas Astron., 25, 337
Döbeli, M., Jones, T., Lee, A., Livi, R., & Tombrello, T. 1991, Radiat. Effects, 118, 325
Draine, B. 1979, Ap&SS, 65, 313
Draine, B., & Salpeter, E. 1977, J. Chem. Phys., 67, 2230
Dresselhaus, M., & Kalish, R. 1992, Ion Implantation in Diamond, Graphite and Related Materials (New York: Springer)
Fegley, B. 1982, Meteoritics, 17, 211
Fleischer, A., Gauger, A., & Sedlmayr, E. 1992, A&A, 266, 321
Frenklach, M., & Feigelson, E. 1989, ApJ, 341, 372
Fryxell, B., Müller, E., & Arnett, D. 1991, ApJ, 367, 619
Fujita, Y., & Tsuji, T. 1977, PASJ, 29, 711
Gustafsson, B. 1989, ARA&A, 27, 701
Haas, M., Colgan, S., Erikson, E., Lord, S., Burton, M., & Hollenbach, D. 1990, ApJ, 360, 257
Herant, M., & Benz, W. 1992, ApJ, 387, 294
Herant, M., & Woosley, S. 1994, ApJ, 425, 814
Hoppe, P., Amari, S., Zinner, E., & Lewis, R. 1995, Geochim. Cosmochim. Acta, 59, 4029
Hoppe, P., Strebel, R., Eberhardt, P., Amari, S., & Lewis, R. 1994, Lunar Planet. Sci., 25, 563
Huggins, P. 1994, Circumstellar Matter 1994, ed. G. Watt & P. Williams, in press
Huss, G., Fahey, A., Gallino, R., & Wasserburg, G. 1994, ApJ, 430, L81
Iben, I. 1991, ApJS, 76, 55
Iben, I., & Renzini, A. 1983, ARA&A, 21, 271
Johnson, D., Friedlander, M., & Katz, J. 1993, ApJ, 407, 714
Joy, D. 1986, in Principles of Analytical Electron Microscopy, ed. D. Joy, A. Romig, & J. Goldstein (New York)
Jura, M., Balm, P., & Kahane, C. 1995, ApJ, 453, 721
Keller, R. 1987, in Polycyclic Aromatic Hydrocarbons and Astrophysics, ed. A. Léger, L. d'Hendecourt, & N. Boccara (Dordrecht: Reidel), 387
Klug, H., & Alexander, L. 1962, X-Ray Diffraction Procedures (New York: Wiley)
Kozasa, T., Hasegawa, H., & Nomoto, K. 1989, ApJ, 344, 325
Kroto, H., Heath, J., O'Brian, S., Curl, R., & Smalley, R. 1985, Nature, 318, 162
Lambert, D., Gustaffson, B., Eriksson, K., & Hinkle, K. 1986, ApJS, 62, 373
Larimer, J. 1975, Geochim. Cosmochim. Acta, 39, 389
Larimer, J., & Bartholomay, M. 1979, Geochim. Cosmochim. Acta, 43, 1453
Lattimer, J., Schramm, D., & Grossman, L. 1978, ApJ, 219, 230
Lewis, J., & Ney, E. 1979, ApJ, 234, 154
Lodders, K., & Fegley, B. 1992, Meteoritics, 27, 250
———. 1993, Meteoritics, 28, 387
———. 1995, Meteoritics, 30, 661
Marchand, A. 1987, in Polycyclic Aromatic Hydrocarbons and Astrophysics, ed. A. Léger, L. d'Hendecourt, & N. Boccara (Dordrecht: Reidel), 31
McDonald, J. 1963, Am. J. Phys., 31, 31
Messenger, S., Alexander, C., Gao, X., Swan, P., Walker, R., Clemett, S., Maechling, C., & Zare, R. 1994, Meteoritics, 29, 502
Meyer, B., Weaver, T., & Woosley, S. 1995, Meteoritics, 30, 325
Miller, J., Mallard, W., & Smyth, K. 1984, J. Phys. Chem., 88, 4963
Nittler, L., Alexander, C., Gao, X., Walker, R., & Zinner, E. 1994, Nature, 370, 443
Nittler, L., et al. 1995, ApJ, 453, L25
Olofsson, H., Eriksson, K., Gustafsson, B., & Carlström, U. 1993, ApJS, 87, 267
Omont, A. 1986, A&A, 164, 159
Ott, U. 1993, Nature, 364, 25
Palla, F., Salpeter, E., & Stahler, S. 1983, ApJ, 271, 632
Podosek, F., Bernatowicz, T., & Kramer, F. 1981, Geochim. Cosmochim. Acta, 45, 2401
Raether, H. 1965, Springer Tracts Mod. Phys., 38, 85

Reimer, L. 1989, Transmission Electron Microscopy (2d ed.; New York: Springer)
Rietmeijer, F., & Mackinnon, I. 1985, Nature, 315, 733
Robertson, J. 1986, Adv. Phys., 35, 317
Robertson, J., & O'Reilly, E. 1987, Phys. Rev. B, 35, 2946
Salpeter, E. 1974a, ApJ, 193, 579
———. 1974b, ApJ, 193, 585
———. 1977, A&A Rev., 15, 267
Samsonov, G. 1974, Refractory Carbides (Studies in Soviet Science: New York: Consultants Bureau)
Sharp, C., & Wasserburg, G. 1995, Geochim. Cosmochim. Acta, 59, 1633
Swan, J., Otto, A., & Fellenzer, H. 1967, Phys. Status Solidi B, 23, 171
Tang, M., & Anders, E. 1988, Geochim. Cosmochim. Acta, 52, 1235
Tsuji, T., Iye, M., Tomioka, K., Okada, T., & Sato, H. 1991, A&A, 252, L1
Ugarte, D. 1992, Nature, 359, 707
Virag, A., Wopenka, B., Amari, S., Zinner, E., Anders, E., & Lewis, R. 1992, Geochim. Cosmochim. Acta, 56, 1715
von Laue, M. 1932, Z. Kristallogr., 82, 127
Warren, B. 1941, Phys. Rev., 59, 693
———. 1990, X-Ray Diffraction (New York: Dover)
Whittet, D., Duley, W., & Martin, P. 1990, MNRAS, 244, 427
Young, K., Phillips, T., & Knapp, G. 1993, ApJ, 409, 725
Zijlstra, A., Loup, C., Waters, L., & de Jong, T. 1992, A&A, 265, L5
Zinner, E., Amari, S., Wopenka, B., & Lewis, R. 1995, Meteoritics, 30, 209
Zuckerman, B., Dyck, H., & Claussen, M. 1986, ApJ, 304, 401

PLATE 16

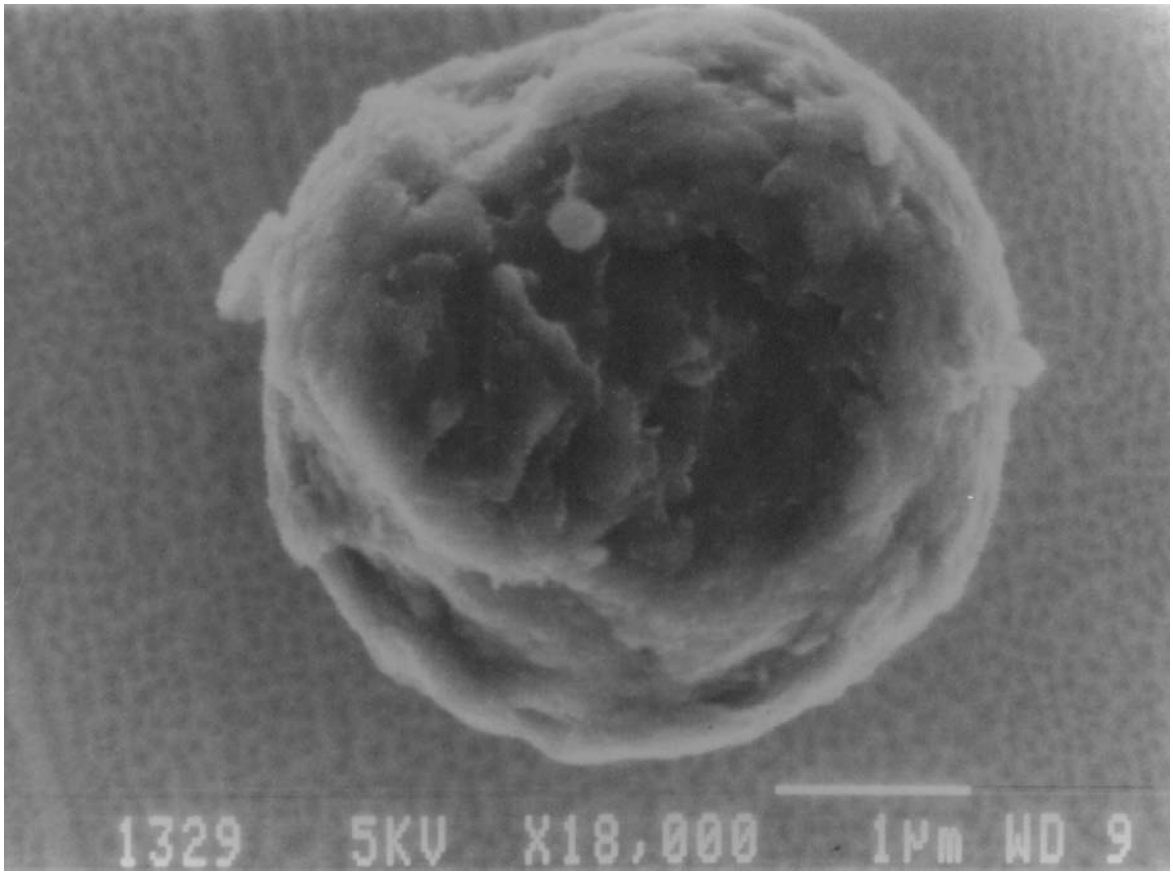

FIG. 2.—Scanning electron microscope image of a typical onion-type circumstellar graphite spherule. Shell-like exterior graphite layers are evident. Scale bar is 1 μm.

BERNATOWICZ et al. (see 472, 762)

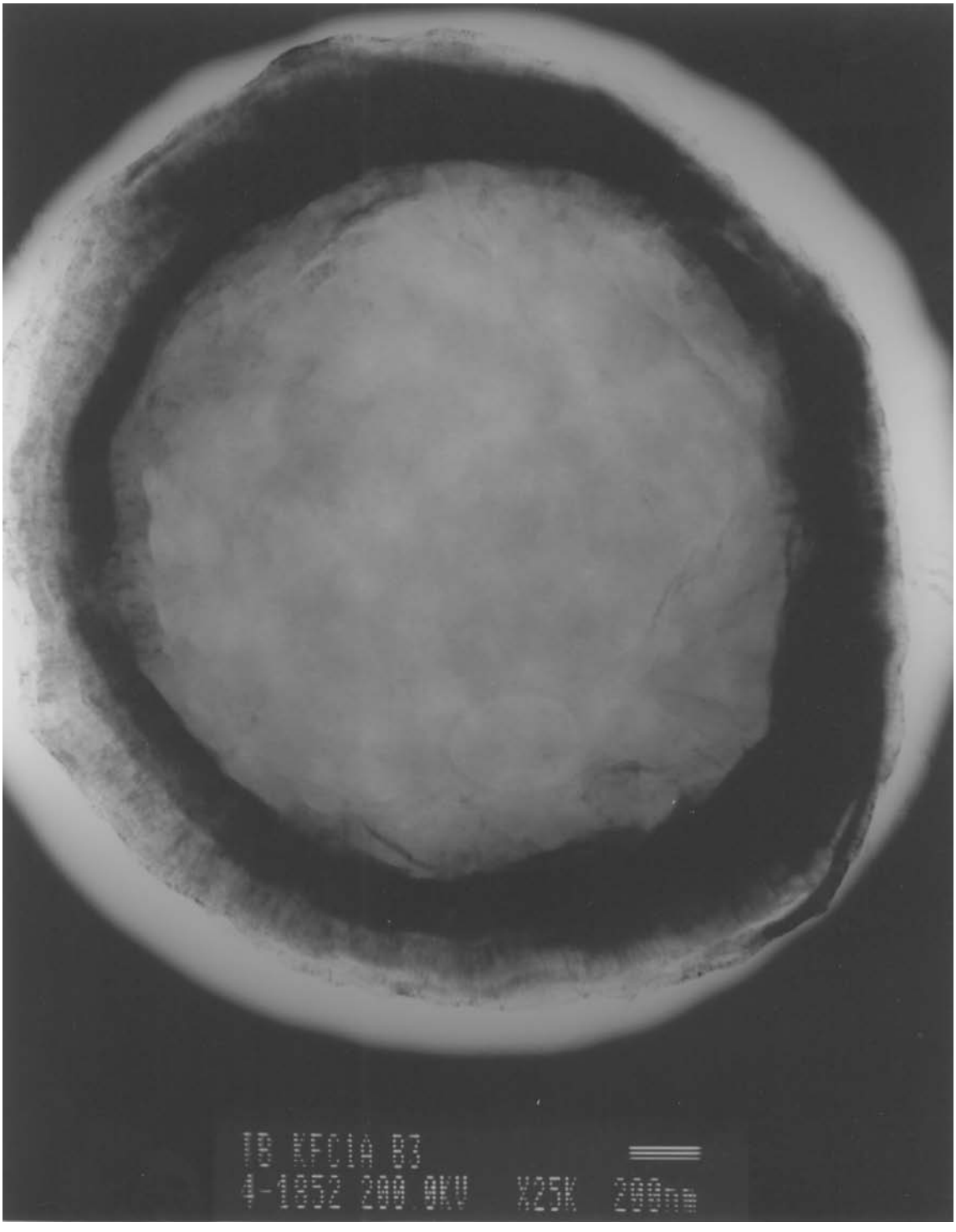

FIG. 3.—TEM bright-field micrograph of a 70 nm thick ultrathin section of an onion-type circumstellar graphite spherule. The outer shell (rim) is well-graphitized carbon that appears dark because of coherent electron scattering from concentric, graphite layering planes. The lighter interior (core) consists of nanocrystalline carbon. Faint oval features visible within the core are holes in the amorphous carbon film supporting the ultrathin section (cf. § 2.1) and are not part of the spherule structure. Scale bar is 200 nm.

BERNATOWICZ et al. (see 472, 763)

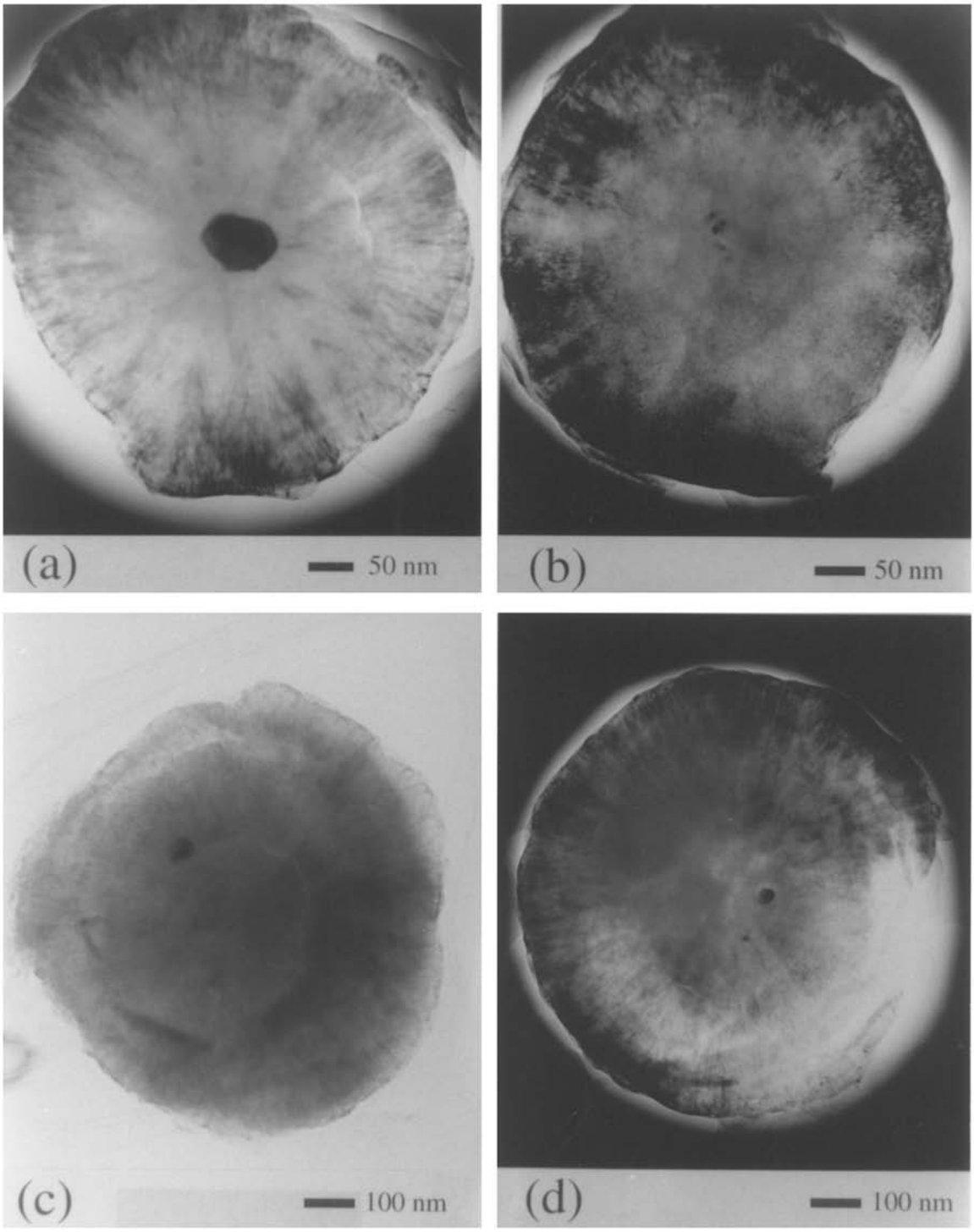

FIG. 7.—TEM bright-field images of ultrathin sections of selected circumstellar graphite spherules with internal crystals (cf. Table 1). (*a*) Spherule B2k, with a large (100 nm) central Fe-rich crystal (Fe or Fe carbide). The dark, radial spokes are a diffraction effect: the graphite layers surrounding the crystal are actually concentric. (*b*) Spherule B2e, with a central cluster of 4 (Ti, Zr, Mo)C crystals. (*c*) Spherule B0g, with a 50 nm noncentral TiC crystal with minor Zr and Mo, and a core of nanocrystalline carbon just interior to this crystal (cf. Fig. 3); this spherule section contains nine other smaller crystals that are not diffracting (hence are not visible) in this orientation. (*d*) Spherule B1w, with two noncentral Ru-, Zr-, and Mo-bearing TiC internal crystals; a third crystal is present but is not visible in this image (cf. Figs. 8 and 9).